# Electron-Rich Piano-Stool Iron *σ*-Acetylides. Electronic Structures of Arylalkynyl Iron(III) Radical Cations†

Frédéric Paul,*,‡ Loic Toupet,§ Jean-Yves Thépot,‡ Karine Costuas,*,∥ Jean-François Halet,∥ and Claude Lapinte‡

*Organométalliques et Catalyse: Chimie et Electrochimie Moléculaires, UMR CNRS 6509, Institut de Chimie, Université de Rennes I, Campus de Beaulieu, Bât. 10C, 35042 Rennes Cedex, France, Groupe Matière Condensée et Matériaux, UMR CNRS 6626, Université de Rennes I, Campus de Beaulieu, 35042 Rennes Cedex, France, and Laboratoire de Chimie du Solide et Inorganique Moléculaire, UMR CNRS 6511, Institut de Chimie, Université de Rennes I, Campus de Beaulieu, 35042 Rennes Cedex, France*

*Received June 21, 2005*

The present study reports the isolation and the structural (X-ray), UV−vis−near-IR, and ESR characterization of a series of Fe(III) complexes of formula $[(\eta^2\text{-dppe})(\eta^5\text{-}C_5Me_5)Fe(C{\equiv}CC_6H_4X)][PF_6]$ (**1a**$[PF_6]$−**1k**$[PF_6]$; with X = $NO_2$, CN, $CF_3$, Br, F, H, Me, $^t$Bu, OMe, $NH_2$, $NMe_2$). The electronic substituent effect of the remote X group on the electronic structure is experimentally evidenced by means of correlations with electronic substituent parameters (ESPs) and is theoretically investigated. The spectroscopic and ESR data are discussed in connection with the DFT computations. A consistent picture of the electronic structure of these Fe(III) radical cations is obtained. Notably, the near-IR absorption observed for **1a**$[PF_6]$−**1k**$[PF_6]$ is assigned to a SOMO-2/SOMO electronic transition.

## Introduction

Mononuclear organometallic acetylide complexes featuring one or several unpaired electrons exhibit usually a very rich chemistry and,[6] when kinetically stable, always constitute a very appealing class of complexes to study from a structural and theoretical viewpoint.[7,8] Nowadays, such species also possess a tremendous potential for molecular electronics, since redox-active organometallic complexes stable under several redox states can be envisioned either as electron or spin reservoirs.[9] This is particularly true for species containing the "$(\eta^2$-dppe$)(\eta^5$-$C_5Me_5)Fe(C{\equiv}C)-$" fragment (dppe = 1,2-bis(diphenylphosphino)ethane),[1−5] owing to the potential these compounds offer for redox switching when incorporated in molecular devices.[10,11] We have indeed shown in several instances that this remarkable fragment allows for efficient switching of various electronic properties of complexes, such as fluorescence[12] and nonlinear optical (NLO) hyperpolarizability.[3] This effect evidently results from the change in redox state of the iron center which is "transmitted" to the rest of the molecule through the alkynyl spacer.

Mononuclear Fe(II) compounds such as $(\eta^2$-dppe$)(\eta^5$-$C_5Me_5)Fe(C{\equiv}CC_6H_4X)$ (**1a**−**k**) have been extensively studied in our group as model complexes to understand the substituent influence on the bonding properties within the metal−acetylide backbone (Chart 1).[1−5,13]

**Chart 1**

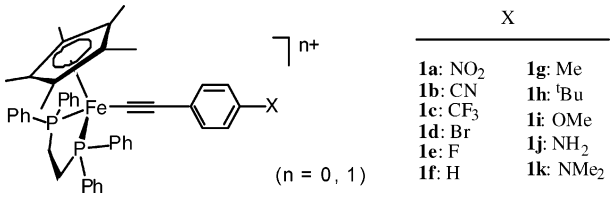


† For previous contributions on similar Fe(II) and Fe(III) alkynyls see refs 1−5.

‡ Organométalliques et Catalyse, UMR CNRS 6509. Tél: (33) 02 23 23 59 62. Fax: (33) 02 23 23 56 37.

§ Groupe Matière Condensée et Matériaux, UMR CNRS 6626. Tél: (33) 02 23 23 64 97. Fax: (33) 02 23 23 52 92.

∥ Laboratoire de Chimie du Solide et Inorganique Moléculaire, UMR CNRS 6511. Tél: (33) 02 23 23 69 73. Fax: (33) 02 23 23 51 98.

(1) Denis, R.; Toupet, L.; Paul, F.; Lapinte, C. *Organometallics* **2000**, *19*, 4240−4251.

(2) Paul, F.; Mevellec, J.-Y.; Lapinte, C. *Dalton Trans.* **2002**, 1783−1790.

(3) Paul, F.; Costuas, K.; Ledoux, I.; Deveau, S.; Zyss, J.; Halet, J.-F.; Lapinte, C. *Organometallics* **2002**, *21*, 5229−5235.

(4) Courmarcel, J.; Le Gland, G.; Toupet, L.; Paul, F.; Lapinte, C. *J. Organomet. Chem.* **2003**, *670*, 108−122.

(5) Costuas, K.; Paul, F.; Toupet, L.; Halet, J.-F.; Lapinte, C. *Organometallics* **2004**, *23*, 2053−2068.

(6) (a) Rigaut, S.; Touchard, D.; Dixneuf, P. H. *Coord. Chem. Rev.* **2004**, *248*, 1585−1601. (b) Le Narvor, N.; Lapinte, C. *J. Chem. Soc., Chem. Commun.* **1993**, 357−359. (c) Beddoes, R. L.; Bitcon, C.; Grime, C. W.; Ricalton, A.; Whiteley, M. W. *J. Chem. Soc., Dalton Trans.* **1995**, 2873−2883. (d) Fernandez, F. J.; Blacque, O.; Alfonso, M.; Berke, H. *Chem. Commun.* **2001**, 1266−1267. (e) Fernandez, F. J.; Venkatesan, K.; Blacque, O.; Alfonso, M.; Schmalle, H.; Berke, H. *Chem. Eur. J.* **2003**, *9*, 6192−6209. (f) Venkatesan, K.; Blacque, O.; Fox, T.; Alfonso, M.; Schmalle, H. W.; Berke, H. *Organometallics* **2004**, *23*, 1183−1186.

(7) (a) Krivykh, V. V.; Eremenko, I. L.; Veghini, D.; Petrunenko, I. A.; Poutney, D. L.; Unseld, D.; Berke, H. *J. Organomet. Chem.* **1996**, *511*, 111−114. (b) Bianchini, C.; Laschi, F.; Masi, D.; Ottaviani, F. M.; Pastor, A.; Peruzzini, M.; Zanello, P.; Zanobini, F. *J. Am. Chem. Soc.* **1993**, *115*, 2723−2730. (c) Beddoes, R. L.; Bitcon, C.; Whiteley, M. W. *J. Organomet. Chem.* **1991**, *402*, 85−96. (d) Doherty, J. C.; Ballem, K. H. D.; Patrick, B. O.; Smith, K. M. *Organometallics* **2004**, *23*, 1487−1489.

(8) Adams, C. J.; Pope, S. J. A. *Inorg. Chem.* **2003**, *43*, 3492−3499.

(9) (a) Venkatesan, K.; Blacque, O.; Fox, T.; Alfonso, M.; Schmalle, H.; Kheradmandan, S.; Berke, H. *Organometallics* **2005**, *24*, 920−932. (b) Astruc, D. *Electron Transfer and Radical Processes in Transition-Metal Chemistry*; VCH: New York, 1995. (c) Kahn, O. *Molecular Magnetism*; VCH: New York, 1993.

(10) Paul, F.; Lapinte, C. *Coord. Chem. Rev.* **1998**, *178/180*, 427−505.

(11) Paul, F.; Lapinte, C. In *Unusual Structures and Physical Properties in Organometallic Chemistry*; Gielen, M., Willem, R., Wrackmeyer, B., Eds.; Wiley: San Francisco, 2002; pp 219−295.

(12) Wong, K. M.-C.; Lam, S. C.-F.; Ko, C.-C.; Zhu, N.; Yam, V. W.-W.; Roué, S.; Lapinte, C.; Fathallah, S.; Costuas, K.; Kahlal, S.; Halet, J.-F. *Inorg. Chem.* **2003**, *42*, 7086−7097.

10.1021/om0505108 CCC: $30.25 
Publication on Web 09/17/2005

**Chart 2**

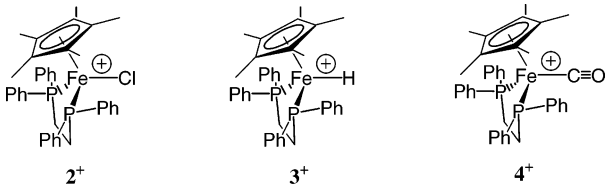

$2^+$ $3^+$ $4^+$

Previous investigations on this particular family of complexes have notably revealed that, depending on the X substituent, sizable changes in local polarization take place for the alkynyl linker before and after oxidation of the Fe(II) center.[2] In addition, it was established that only minor geometrical changes could be expected upon mono-oxidation and a dominant iron-centered structure was proposed for this radical species.[5] However, only limited experimental data were available for the Fe(III) parents.[14] Considering that such stable organometallic piano-stool radical cations are reasonably scarce species and deserve some special interest,[15−17] and also in order to better understand the influence of the oxidation upon the electronic properties of such electron-rich Fe(II) acetylides,[18−20] we have now isolated here the complete family of corresponding radical Fe(III) cations [($\eta^2$-dppe)($\eta^5$-$C_5Me_5$)Fe(C≡$CC_6H_4$X)][$PF_6$] (**1a**[$PF_6$]−**1k**[$PF_6$]) from **1a**−**k** (Chart 1).

We thus complete here the spectroscopic characterization of these Fe(III) alkynyl complexes by means of electron spin resonance (ESR) and ultraviolet−visible (UV−vis) and near-infrared (near-IR) spectroscopy,[19,20] as well as the solid-state structures and the magnetic measurements (Evans method) for selected representatives. The electronic structures of the entire Fe(III) family are discussed with complementary density functional theory calculations (DFT). To determine the impact of the acetylide ligand on these properties, we also gathered data for closely related mononuclear complexes without such a ligand, i.e., the known chloro and hydride complexes [($\eta^2$-dppe)($\eta^5$-$C_5Me_5$)FeCl][$PF_6$] (**2**[$PF_6$])[21] and [($\eta^2$-dppe)($\eta^5$-$C_5Me_5$)FeH][$PF_6$] (**3**[$PF_6$])[22] (Chart 2).[23] Actually, the present contribution constitutes a logical continuation of the previous theoretical/experimental investigation on the corresponding Fe(II) congeners[5] and also usefully complements an older contribution from some of us on closely related σ-alkyl Fe(III) complexes.[21]

**Scheme 1**

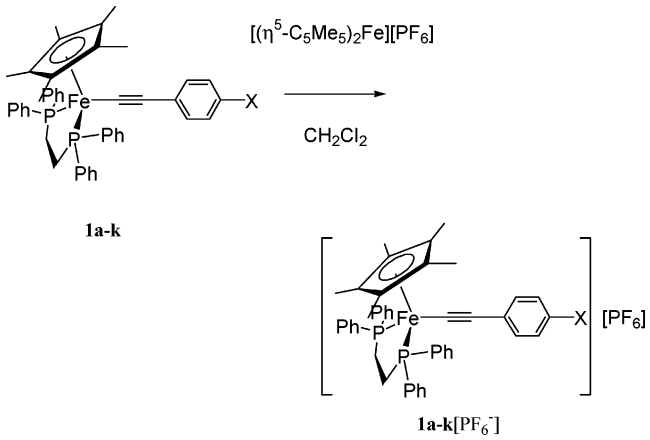


## Results

**Synthesis and Solid-State Structures.** The complexes **1a**[$PF_6$]−**1k**[$PF_6$] (X = $NO_2$, CN, $CF_3$, F, Br, H, Me, $^t$Bu, OMe, $NH_2$, $NMe_2$) were isolated after chemical oxidation of their known Fe(II) parents using ferrocenium hexafluorophosphate, following the workup previously given for the complexes with the nitro (**1a**) and amino (**1j**) substituents (Scheme 1).[1] The isolated samples were characterized by infrared spectroscopy. Their purity was checked by cyclic voltammetry, and satisfactory elemental analyses were obtained in most cases. Notably, we have shown recently that the cationic carbonyl complex $4^+$ (Chart 2) forms quantitatively upon reaction of molecular oxygen with **1a**[$PF_6$]−**1k**[$PF_6$], the reaction being favored by electron-releasing substituents.[24] Clearly, these Fe(III) radical cations, although isolable at ambient temperature, are still quite reactive species and should be checked periodically when stored.

In addition to **1a**[$PF_6$], previously characterized by X-ray diffraction,[1] crystals could be grown for several other representatives (X = CN, Br, H, Me, $^t$Bu, OMe, $NH_2$) and their solid-state structures were solved (Figure 1 and Tables 1 and 2). As reported for **1a**[$PF_6$], all complexes crystallize in the monoclinic systems ($P2_1/n$ space groups in most cases) with one molecule per asymmetric unit, except for **1f**[$PF_6$]. The latter crystallizes in the orthorhombic system and presents two molecules in the asymmetric unit. We also unexpectedly realized with **1b**[$PF_6$] that some of these Fe(III) complexes could be stable toward water; two water molecules act as solvates in this particular case.

In comparison to the Fe(II) parents, the geometrical changes reveal the expected expansion of the coordination sphere of the iron center upon oxidation. For the complete series of Fe(III) compounds, only very slight geometrical differences take place in the aryl acetylide fragment when X is varied. The bond length with the

(13) Denis, R.; Weyland, T.; Paul, F.; Lapinte, C. *J. Organomet. Chem.* **1997**, *545/546*, 615−618.
(14) Connelly, N. G.; Gamasa, M. P.; Gimeno, J.; Lapinte, C.; Lastra, E.; Maher, J. P.; Le Narvor, N.; Rieger, A. L.; Rieger, P. H. *J. Chem. Soc., Dalton Trans.* **1993**, 2575−2578.
(15) (a) Smith, K. M. *Organometallics* **2004**, *24*, 778−784. (b) Legzdins, P.; McNeil, W. S.; Batchelor, R. J.; Einstein, F. W. B. *J. Am. Chem. Soc.* **1995**, *117*, 54−66. (c) Le Bras, J.; Jiao, H.; Meyer, W. E.; Hampel, F.; Gladysz, J. A. *J. Organomet. Chem.* **2000**, *616*, 54−66 and references therein.
(16) (a) Fortier, S.; Baird, M. C.; Morton, K. F. P. J. R.; Ziegler, T.; Jaeger, T. J.; Watkins, W. C.; MacNeil, J. H.; Watson, K. A.; Hensel, K.; Le Page, Y.; Charland, J.-P.; Williams, A. J. *J. Am. Chem. Soc.* **1991**, *113*, 542−551. (b) Pike, R. D.; Rieger, A. L.; Rieger, P. H. *J. Chem. Soc., Faraday Trans. 1* **1989**, *85*, 3913−3925.
(17) Cooley, N. A.; Baird, M. C.; Morton, J. R.; Preston, K. F.; Le Page, Y. *J. Magn. Reson.* **1988**, *76*, 325−330.
(18) Weyland, T.; Costuas, K.; Mari, A.; Halet, J.-F.; Lapinte, C. *Organometallics* **1998**, *17*, 5569−5579.
(19) Le Stang, S.; Paul, F.; Lapinte, C. *Inorg. Chim. Acta* **1999**, *291*, 403−425.
(20) Weyland, T.; Costuas, K.; Toupet, L.; Halet, J.-F.; Lapinte, C. *Organometallics* **2000**, *19*, 4228−4239.
(21) Roger, C.; Hamon, P.; Toupet, L.; Rabaâ, H.; Saillard, J.-Y.; Hamon, J.-R.; Lapinte, C. *Organometallics* **1991**, *10*, 1045−1054.
(22) Hamon, P.; Hamon, J.-R.; Lapinte, C. *J. Chem. Soc., Chem. Commun.* **1992**, 1602−1603.
(23) (a) Tilset, M.; Fjeldahl, I.; Hamon, J.-R.; Hamon, P.; Toupet, L.; Saillard, J.-Y.; Costuas, K.; Haynes, A. *J. Am. Chem. Soc.* **2001**, *123*, 9984−10000. (b) Tilset, M.; Hamon, J.-R.; Hamon, P. *Chem. Commun.* **1998**, 765−766.
(24) Paul, F.; Toupet, L.; Roisnel, T.; Hamon, P.; Lapinte, C. *C. R. Chim.* **2005**, *8*, 1174−1185.

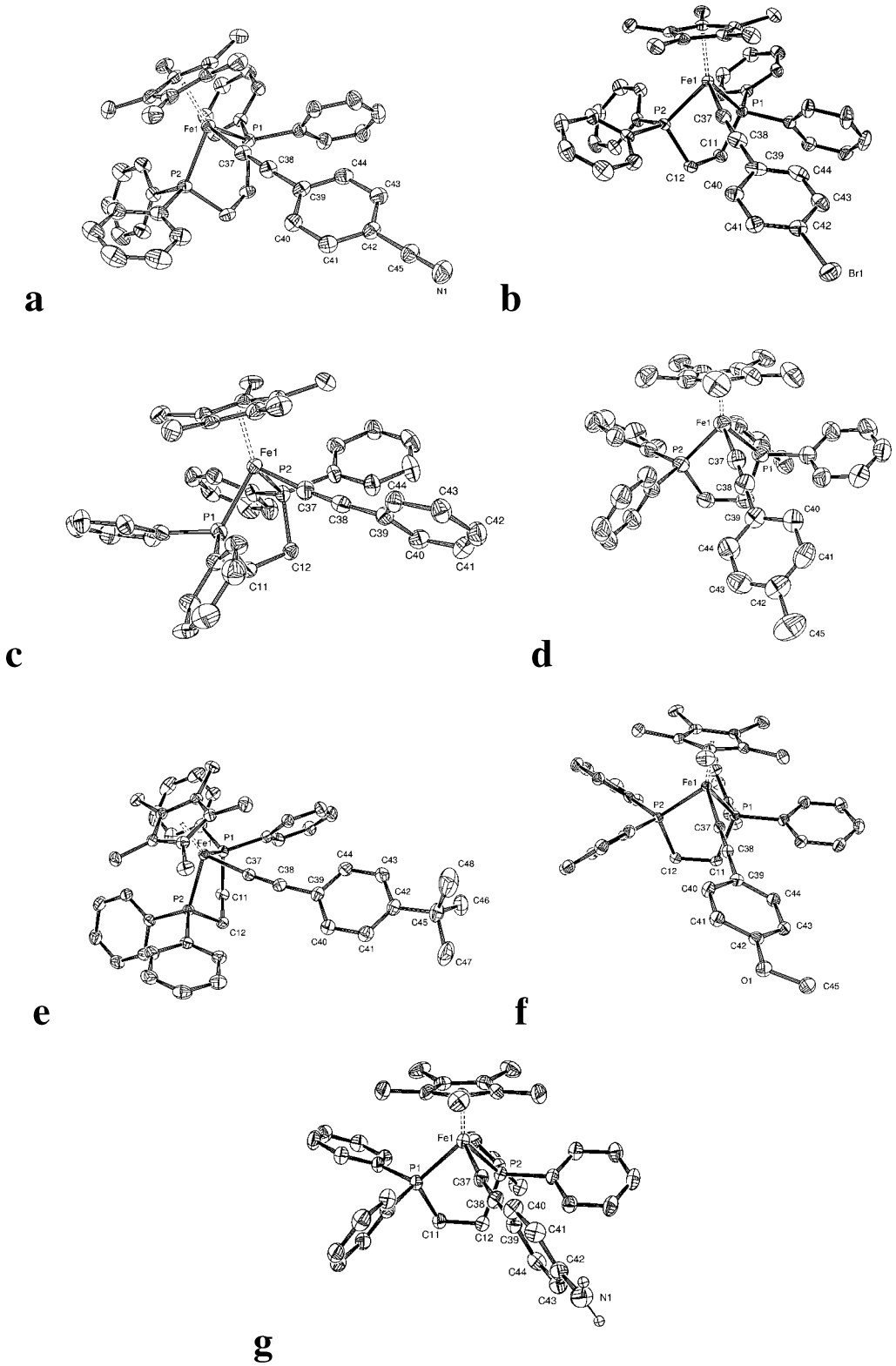


**Figure 1.** ORTEP representations of the complexes **1b**[$PF_6$] (a), **1d**[$PF_6$] (b), **1f**[$PF_6$] (c), **1g**[$PF_6$] (d), **1h**[$PF_6$] (e), **1i**[$PF_6$] (f), and **1j**[$PF_6$] (g) at the 50% probability level ($PF_6^-$ counterions not shown).

substituent (C42−X) relative to that in the corresponding Fe(II) parent changes significantly only in the case of the amino complex **1j**[$PF_6$] (1.370(6) vs 1.406(5) Å). This shortening is in contrast with the lengthening previously stated for **1a**[$PF_6$][1] and could now originate from an increased $\pi$-bonding between the amine center and the aryl ring in the Fe(III) complex. The changes in this bond length for other complexes are not really significant (1.435(5) vs 1.441(8) Å, 1.904(4) vs 1.904(4) Å, 1.510(7) vs 1.512(4) Å, and 1.370(3) vs 1.382(3) Å for X = CN, Br, $CH_3$, OMe, respectively). The C≡N bond of the cyano substituent appears also quite affected by oxidation (1.152(5) vs 1.130(7) Å).[26a] Finally, considering only the complexes crystallizing in the $P2_1/n$ space

(25) Szafert, S.; Gladysz, J. *Chem. Rev.* **2003**, *103*, 4175−4205.

**Table 1. Crystal Data and Data Collection and Refinement Parameters for 1b[$PF_6$], 1d[$PF_6$], 1f[$PF_6$], 1g[$PF_6$], 1h[$PF_6$], 1i[$PF_6$], and 1j[$PF_6$]**

| | **1b**$^+$ (X = CN) | **1d**$^+$ (X = Br) | **1f**$^+$ (X = H) | **1g**$^+$ (X = Me) | **1h**$^+$ (X = $^t$Bu) | **1i**$^+$ (X = OMe) | **1j**$^+$ (X = $NH_2$) |
|---|---|---|---|---|---|---|---|
| formula | $C_{45}H_{43}NP_2Fe(PF_6)\cdot 2H_2O$ | $C_{44}H_{43}BrP_2Fe(PF_6)\cdot CH_3OH$ | $C_{88}H_{88}F_{12}P_4Fe_2(2PF_6)$ | $C_{45}H_{46}P_2Fe(PF_6)$ | $C_{48}H_{52}P_2Fe(PF_6)$ | $C_{45}H_{46}OP_2Fe(PF_6)$ | $C_{44}H_{45}NP_2Fe(PF_6)\cdot CH_2Cl_2$ |
| fw | 896.6 | 946.50 | 1671.10 | 849.58 | 891.66 | 865.58 | 935.50 |
| temp (K) | 120(2) | 120(2) | 120(1) | 293(2) | 120(1) | 120(1) | 120(2) |
| cryst syst | monoclinic | monoclinic | orthorhombic | monoclinic | monoclinic | monoclinic | monoclinic |
| space group | $P2_1/n$ | $P2_1/n$ | $Pca2_1$ | $C2/c$ | $P2_1/n$ | $P2_1/n$ | $P2_1/n$ |
| $a$ (Å) | 15.2639(3) | 15.3126(2) | 25.1849(4) | 27.4521(6) | 11.7138(1) | 14.0681(3) | 13.0259(2) |
| $b$ (Å) | 16.6781(3) | 16.3293(2) | 16.6927(3) | 13.0301(3) | 21.1255(2) | 17.2547(3) | 15.1369(3) |
| $c$ (Å) | 16.5813(3) | 16.7496(2) | 18.8160(4) | 23.5369(4) | 17.4624(2) | 17.0021(3) | 23.4141(5) |
| α (deg) | 90.0 | 90.0 | 90.0 | 90.0 | 90.0 | 90.00 | 90.0 |
| $\beta$ (deg) | 93.128(1) | 94.382(1) | 90.0 | 92.237(1) | 94.087(1) | 100.594(1) | 105.934(1) |
| $\gamma$ (deg) | 90.0 | 90.0 | 90.0 | 90.0 | 90.0 | 90.00 | 90.0 |
| $V$ (Å$^3$) | 4214.9(1) | 4175.9(1) | 7910.3(3) | 8417.3(3) | 4321.24(7) | 4056.76(13) | 4439.22(15) |
| $Z$ | 4 | 4 | 4 | 8 | 4 | 4 | 4 |
| $D_{calcd}$ (g cm$^{-3}$) | 1.413 | 1.495 | 1.403 | 1.341 | 1.371 | 1.417 | 1.400 |
| cryst size (mm) | 0.42 × 0.40 × 0.35 | 0.22 × 0.15 × 0.12 | 0.42 × 0.32 × 0.30 | 0.50 × 0.35 × 0.35 | 0.40 × 0.32 × 0.30 | 0.44 × 0.34 × 0.31 | 0.30 × 0.30 × 0.12 |
| $F$(000) | 1860 | 1940 | 3464 | 3528 | 1860 | 1796 | 1932 |
| diffractometer (Nonius) | Kappa CCD | Kappa CCD | Kappa CCD | Kappa CCD | Kappa CCD | Kappa CCD | Kappa CCD |
| radiation | Mo Kα | Mo Kα | Mo Kα | Mo Kα | Mo Kα | Mo Kα | Mo Kα |
| abs coeff (mm$^{-1}$) | 0.537 | 1.495 | 0.563 | 0.530 | 0.520 | 0.553 | 0.626 |
| data collection | | | | | | | |
| $2\theta_{max}$ (deg) | 54 | 54 | 54 | 54 | 54 | 54 | 54 |
| no. of frames | 227 | 117 | 186 | 225 | 262 | 122 | 203 |
| Ω rotation (deg) | 2.0 | 2.0 | 1.2 | 1.4 | 1.6 | 2.0 | 1.5 |
| scan rate (s/frame) | 20 | 80 | 25 | 12 | 110 | 30 | 73 |
| $\theta$ range (deg) | 1.73−27.48 | 2.14−27.47 | 1.22−27.48 | 1.48−27.47 | 2.25−27.54 | 1.70−27.52 | 1.62−27.48 |
| $hkl$ ranges | 0−19 | 0−19 | 0−32 | 0−35 | 0−15 | 0−18 | 0−16 |
| | 0−21 | 0−21 | 0−21 | 0−16 | 0−22 | 0−22 | 0−19 |
| | −21 to +21 | −21 to +21 | 0−24 | −30 to +30 | −27 to +27 | −22 to +22 | −30 to +29 |
| total no. of rflns | 69 005 | 39 693 | 59 451 | 40 464 | 76 089 | 41 000 | 51 541 |
| no. of unique rflns | 9636 | 9536 | 9340 | 9571 | 19 482 | 9309 | 10 175 |
| no. of obsd rflns ($I > 2\sigma(I)$) | 7353 | 7986 | 7217 | 4798 | 9916 | 7362 | 6523 |
| no. of restraints/params | 0/514 | 0/513 | 0/973 | 0/506 | 0/524 | 0/506 | 0/529 |
| $w = 1/[\sigma^2(F_o)^2 + (aP)^2 + bP]^a$ | $a = 0.0920$ | $a = 0.0826$ | a = 0.1266 | $a = 0.1143$ | $a = 0.0656$ | $a = 0.0657$ | $a = 0.1120$ |
| | $b = 12.6000$ | $b = 22.2426$ | $b = 3.8822$ | b = 0.0000 | $b = 3.1905$ | $b = 3.8619$ | $b = 5.9585$ |
| final $R$ | 0.0664 | 0.0681 | 0.0713 | 0.0670 | 0.0435 | 0.0449 | 0.0712 |
| final $R_w$ | 0.1690 | 0.1704 | 0.1687 | 0.1752 | 0.1180 | 0.1146 | 0.1840 |
| $R$ (all data) | 0.0903 | 0.0818 | 0.0993 | 0.1540 | 0.0497 | 0.0634 | 0.1211 |
| $R_w$ (all data) | 0.1904 | 0.1821 | 0.1921 | 0.2176 | 0.1236 | 0.1277 | 0.2158 |
| goodness of fit/$F^2$ ($S_w$) | 1.008 | 0.994 | 1.073 | 1.020 | 1.022 | 1.024 | 1.042 |
| $\Delta\rho_{max}$ (e Å$^{-3}$) | 1.2 | 2.8 | 1.8 | 0.56 | 0.86 | 0.65 | 1.85 |
| largest diff peak, hole (e Å$^{-3}$) | 1.824, −1.258 | 2.816, 2.467 | 2.821, −0.557 | 0.564, −0.463 | 0.867, −0.526 | 0.652, −0.679 | 1.850, −0.871 |

$^a P = [F_o^2 + F_c^2]/3$.

group, the data reveal a noticeable deviation from linearity of the Fe−C≡C fragment when the X substituent becomes more and more electron-releasing.

As discussed in our previous contribution on these compounds,[5] the structural features experimentally determined for the Fe(III) complexes are overall in good accordance with the optimized geometries that were computed for the corresponding model complexes by means of density functional theory (DFT). Notably, the trend found for the C42−X bond length is well in line with theoretical computations previously reported.[5,26b] The largest discrepancies are presently observed for **1f**[$PF_6$]. Note, however, that these experimental values were obtained with relatively large uncertainties. Moreover, since **1f**[$PF_6$] presents two molecules in the asymmetric unit, this discrepancy could also originate from solid-state effects induced by the unusual packing of this complex.[25] We now have closely examined the Fe−C37−C38 and the C37−C38−C39 angles in DFT-computed structures obtained for **1a**-H$^+$−**1k**-H$^+$ from optimization, to see if the acetylide "bending" experimentally observed could have a intramolecular origin. No clear trend was apparent from theoretical data, most angles being quite close to 180°.

**Evans Measurements.** Evans measurements were performed on selected Fe(III) complexes in chloroform or in dichloromethane (Table 3). The Fe(III) compounds proved to decompose slowly in chloroform solutions, especially with electron-releasing X substituents, and the measurements had to be performed rapidly after dissolution of the complexes. With several of these

(26) (a) For the cyano complex (**1b**[$PF_6$]), the $\nu_{CN}$ value observed in the solid-state infrared spectrum of this complex suggests that the cyano bond is strengthened upon oxidation, not weakened. A shortening and not a lengthening of this bond should therefore be observed in the crystal structure. Whether this discrepancy is an artifact originating from the comparably large uncertainty in these bond lengths or results from a specific vibronic coupling involving the CN unit is presently unknown. (b) We thank a reviewer for this interesting comment.

**Table 2. Selected Bond Lengths (Å) and Angles (deg) for 1b[PF$_6$], 1d[PF$_6$], 1f[PF$_6$], 1g[PF$_6$], 1h[PF$_6$], 1i[PF$_6$], and 1j[PF$_6$]**

| | **1b** (X = CN) | **1d** (X = Br) | **1f** (X = H) | **1g** (X = Me) | **1h** (X = $^t$Bu) | **1i** (X = OMe) | **1j** (X = NH$_2$) |
|---|---|---|---|---|---|---|---|
| | | | Selected Bond Lengths | | | | |
| Fe−(Cp*)$_{centroid}$ | 1.774 | 1.779 | 1.766/1.784 | 1.772 | 1.773 | 1.776 | 1.773 |
| Fe−P1 | 2.2739(10) | 2.2640(11) | 2.2599(18)/2.2266(19) | 2.2595(11) | 2.2718(5) | 2.2402(6) | 2.2497(11) |
| Fe−P2 | 2.2554(10) | 2.2519(11) | 2.2535(19)/2.2453(18) | 2.2682(13) | 2.2484(5) | 2.2628(6) | 2.2355(12) |
| Fe−C37 | 1.892(4) | 1.876(4) | 1.919(7)/1.852(7) | 1.889(4) | 1.891(2) | 1.895(2) | 1.865(4) |
| C37−C38 | 1.219(5) | 1.230(7) | 1.207(10)/1.262(10) | 1.207(6) | 1.218(3) | 1.220(3) | 1.219(6) |
| C38−C39 | 1.443(5) | 1.431(6) | 1.438(10)/1.425(10) | 1.438(6) | 1.443(3) | 1.436(3) | 1.432(6) |
| C39−C40 | 1.405(5) | 1.410(6) | 1.412(10)/1.396(10) | 1.390(6) | 1.396(3) | 1.408(3) | 1.407(6) |
| C40−C41 | 1.378(5) | 1.382(6) | 1.373(10)/1.363(11) | 1.391(6) | 1.385(3) | 1.382(3) | 1.379(6) |
| C41−C42 | 1.397(5) | 1.381(6) | 1.385(10)/1.402(11) | 1.359(7) | 1.399(3) | 1.396(3) | 1.387(6) |
| C42−C43 | 1.397(5) | 1.386(6) | 1.375(11)/1.384(11) | 1.383(7) | 1.397(3) | 1.387(4) | 1.420(6) |
| C43−C44 | 1,390(5) | 1.379(7) | 1.396(11)/1.375(10) | 1.370(7) | 1.375(3) | 1.393(3) | 1.355(6) |
| C44−C39 | 1.398(5) | 1.403(7) | 1.360(10)/1.406(9) | 1.383(7) | 1.408(3) | 1.398(3) | 1.407(6) |
| C42−X | 1.435(5) | 1.904(4) | / | 1.510(7) | 1.536(3) | 1.370(3) | 1.370(6) |
| X−Y1 | 1.152(5) | | | | 1.547(4) | 1.431(3) | |
| X−Y2 | | | | | 1.530(4) | | |
| X−Y3 | | | | | 1.545(4) | | |
| | | | Selected Bond Angles | | | | |
| P1−Fe−P2 | 83.53(3) | 83.36(4) | 83.18(7)/84.71(7) | 84.27(4) | 83.801(19) | 82.37(2) | 84.69(4) |
| P1−Fe−C37 | 90.06(11) | 90.52(14) | 85.8(2)/90.6(2) | 84.36(12) | 89.24(6) | 86.84(7) | 90.65(13) |
| P2−Fe−C37 | 84.21(11) | 84.87(13) | 89.2(2)/86.3(2) | 87.71(14) | 85.38(6) | 90.67(7) | 84.93(12) |
| Fe−C37−C38 | 175.6(3) | 174.1(4) | 171.0(6)/174.5(6) | 176.8(4) | 174.29(17) | 171.0(2) | 171.9(4) |
| C37−C38−C39 | 176.2(4) | 177.6(6) | 176.2(8)/175.2(7) | 176.0(5) | 174.7(2) | 176.7(2) | 176.2(5) |
| C40−C39−C44 | 119.2(3) | 118.0(4) | 118.6(7)/119.4(7) | 117.8(4) | 117.67(19) | 117.9(2) | 117.0(4) |
| C41−C42−C43 | 120.5(3) | 122.7(4) | 120.3(7)/119.4(7) | 117.4(4) | 117.5(2) | 120.1(2) | 117.8(4) |
| C41−C42−X | 120.2(3) | 120.0(3) | | 121.7(5) | 122.9(2) | 115.8(2) | 121.1(4) |
| C43−C42−X | 119.4(3) | 117.3(4) | | 120.9(6) | 119.7(2) | 124.1(2) | 120.9(4) |
| C42-X−Y1 | 178.8(5) | | | | 109.9(2) | 117.1(2) | |
| C42-X−Y2 | | | | | 111.9(2) | | |
| C42-X−Y3 | | | | | 108.4(2) | | |
| Fe−(Cp*)$_{centroid}$/C39−C40[a] | 91.6 | 90.3 | 41.0/38.3 | 62.3 | 95.5 | 96.7/10.6[b] | 23.6/0[b] |

[a] Dihedral angle (Cp* = pentamethylcyclopentadienyl ligand). [b] Dihedral angle (aryl mean plane)/(substituent mean plane or axis).

**Table 3. Experimental Molecular Magnetic Moments (in $\mu_B$) from Evans Measurements in CDCl$_3$ at 297 K for Selected Compounds among 1a[PF$_6$]−1k[PF$_6$]**

| | [Fe]C≡C(C$_6$H$_4$)X | | | | |
|---|---|---|---|---|---|
| | X = NO$_2$ | X = CN | X = H | X = OMe | X = NH$_2$ |
| $\mu$ ($\mu_B$) | 1.57 | 1.45[b] | 1.87 | 1.56[a,b] | 1.16[b] |

[a] In $CD_2Cl_2$. [b] Slight decomposition observed in the NMR tube.

samples, partial decomposition could not be avoided during the measurements, and generated signals for an unidentified side product (less than 20% in general). The latter likely corresponds to the diamagnetic Fe(II) complex **4**[PF$_6$] (Chart 2).[24] With respect to the experimental uncertainties associated with these measurements, the paramagnetic complexes apparently show a molecular magnetic moment close to 1.7 $\mu_B$, which corresponds to the spin-only value calculated for one unpaired electron. Thus, as expected from previous investigations,[10,14] this establishes that these Fe(III) derivatives are low-spin complexes in solution and that the unpaired electron experiences only a slight spin−orbit coupling.

**ESR Measurements.** ESR measurements on the **1a**[PF$_6$]−**1k**[PF$_6$] radicals were performed in 1,2-dichloroethane/dichloromethane (1:1) in frozen glasses at 77 K. Under such conditions, rhombic spectra were obtained for all compounds (Table 4). The Fe(III) radical cations were either generated in situ from neutral Fe(II) complexes or obtained from isolated Fe(III) complexes. In contrast to a previous ESR investigation on similar compounds, no hyperfine structure corresponding to a coupling to equivalent $^{31}$P atoms could be resolved.[14] Given the relative width of the observed features, such a coupling (ca. 15−20 G) could easily be concealed underneath. Notably, for all complexes, a significantly larger half-width is observed for the low-field component of the **g** tensor (ca. 70 vs ca. 30 G). A similar observation was also made by Rieger and coworkers on the isoelectronic radical ($\eta^6$-C$_6$Me$_6$)Cr(PEt$_3$)(CO)$_2$ a few years ago, and an explanation was proposed for this phenomenon.[27] More importantly, it appears clearly that the anisotropy ($\Delta g$) of the ESR spectra increases with the electron-withdrawing capability of the X substituent.

**Table 4. ESR Spectroscopic Data[a] for [($\eta^2$-dppe)($\eta^5$-C$_5$Me$_5$)FeC≡CAr][PF$_6$] Complexes**

| Ar | $g_1$ | $g_2$ | $g_3$ | $\Delta$g | $\langle g \rangle$ | ref |
|---|---|---|---|---|---|---|
| *p*-(C$_6$H$_4$)NO$_2$ | 1.973 | 2.028 | 2.497 | 0.524 | 2.167 | this work |
| *p*-(C$_6$H$_4$)CN | 1.970 | 2.028 | 2.499 | 0.529 | 2.166 | this work |
| *p*-(C$_6$H$_4$)CF$_3$ | 1.970 | 2.028 | 2.496 | 0.527 | 2.165 | this work |
| *p*-(C$_6$H$_4$)Br | 1.974 | 2.034 | 2.475 | 0.501 | 2.161 | this work |
| *p*-(C$_6$H$_4$)F | 1.976 | 2.032 | 2.448 | 0.472 | 2.152 | this work |
| *p*-(C$_6$H$_5$) | 1.975 | 2.033 | 2.464 | 0.489 | 2.157 | 14 |
| *p*-(C$_6$H$_4$)Me | 1.979 | 2.034 | 2.424 | 0.445 | 2.145 | this work |
| *p*-(C$_6$H$_4$)$^t$Bu | 1.978 | 2.032 | 2.444 | 0.466 | 2.151 | this work |
| *p*-(C$_6$H$_4$)OMe | 1.983 | 2.036 | 2.379 | 0.396 | 2.133 | this work |
| *p*-(C$_6$H$_4$)NH$_2$ | 1.992 | 2.037 | 2.310 | 0.318 | 2.113 | this work |
| *p*-(C$_6$H$_4$)NMe$_2$ | 1.993 | 2.039 | 2.263 | 0.270 | 2.098 | this work |
| Cl | 1.987 | 2.055 | 2.454 | 0.467 | 2.165 | this work |
| H | 1.994 | 2.043 | 2.449 | 0.455 | 2.162 | 23a |

[a] At 77 K in a $CH_2Cl_2$−$C_2H_4Cl_2$ (1:1) glass.

Variable-temperature measurements performed on **1a**[PF$_6$], **1f**[PF$_6$], **1i**[PF$_6$], and **1j**[PF$_6$] reveal that any signal is lost in solution, above 180 K for the first two

(27) Castellani, M. P.; Connelly, N. G.; Pike, R. D.; Rieger, A. L.; Rieger, P. H. *Organometallics* **1997**, *16*, 4369−4376.

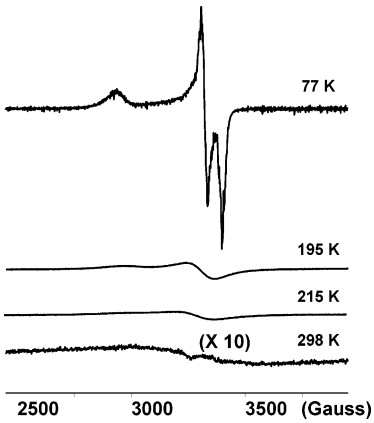


**Figure 2.** Variable-temperature ESR spectra of the **1j**[$PF_6$] radical (X = $NH_2$) in 1,2-$CH_2Cl_2$/$C_2H_4Cl_2$ (1:1). Please note the changes in relative intensity (the spectrum at 77 K was recorded with half of the accumulations of the other spectra).

compounds. On the other hand, in the last two cases, a very weak (ca. 200 times less intense) and large isotropic signal is still observable at ambient temperature at $g$ = 2.007, 2.088, respectively, with a peak-to-peak separation of ca. 500 G (Figure 2). This suggests that spin relaxation might be somewhat slower with the more electron-releasing substituents in this series of compounds. As shown in Figure 2, upon heating, the rhombic signal transforms transiently in a pseudoaxial signal around 190 K, before giving a large and weak isotropic signal above 220 K, upon melting of the solvent glass. This behavior is reminiscent of that observed with related piano-stool $d^5$ radicals such as ($\eta^5$-$C_5Ph_5$)Cr($PMe_3$)$(CO)_2$, which was previously attributed to the rotation of the ligand along the main $g$-component axis in the melting solvent glass.[28] The relative constancy of the average $g$ value upon variation of the temperature shows that the spectral changes are due neither to the presence of more than one paramagnetic species in the sample nor to a change in spin state.[29]

Under similar conditions, the ESR spectra of the known [($\eta^2$-dppe)($\eta^5$-$C_5Me_5$)FeCl][$PF_6$] (**2**[$PF_6$]) and [($\eta^2$-dppe)($\eta^5$-$C_5Me_5$)FeH][$PF_6$] (**3**[$PF_6$]) radical cations were also recorded.[23a] The Fe(III) hydride complex **3**[$PF_6$] is unstable in the solvent system used and transforms into another unknown metal-centered radical species, exhibiting three tensors at $g$ = 2.002, 2.044, 2.339 with a lesser anisotropy ($\Delta g$ = 0.337). This is not very surprising, considering the instability already reported for the Fe(II) hydride parent in dichloromethane.[30]

**Electronic Spectroscopy.** Electronic spectroscopy can provide a wealth of information on the electronic structure of radical cations. We therefore recorded the electronic spectra of **1a**[$PF_6$]−**1k**[$PF_6$] in dichloromethane solutions, in the UV−vis (Table 5) and in the near-infrared (near-IR) range (Table 6). The UV−vis spectra presented several absorptions which were found for all Fe(III) acetylide complexes (Figure 3). Thus, for **1a**[$PF_6$]−**1j**[$PF_6$], two distinct peaks are apparent in the 600−850 nm spectral range and only one for **1k**[$PF_6$]. These are bathochromically shifted and gain in intensity as the X substituent becomes more and more electron releasing. The substituent effect is opposite to the trend previously reported for the corresponding Fe(II) parents[5] and would be in favor of these transitions being LMCT in character. For the chloro (**2**[$PF_6$]) and hydride Fe(III) complexes (**3**[$PF_6$]), the low-energy absorptions resemble those of the complex **1a**[$PF_6$] but are blue-shifted relative to them and present lower extinction coefficients.[31]

Measurements in the near-IR range indicate that most Fe(III) radicals were generated in situ from the neutral Fe(II) parents using ferrocenium hexafluorophosphate as an oxidant, but we checked for several representatives (**1a**[$PF_6$], **1f**[$PF_6$], **1i**[$PF_6$], **1k**[$PF_6$], and **3**[$PF_6$]) that similar spectra are obtained from isolated Fe(III) samples. A weak absorption is detected for all acetylide complexes **1a**[$PF_6$]−**1k**[$PF_6$] in the 1500−2000 nm range. As observed with **1a**[$PF_6$] or **1f**[$PF_6$], the extinction coefficient of this electronic absorption was not sensitive to dilution, in line with its intramolecular nature, nor to the nature of the solvent used (see the Supporting Information). This absorption is, however, quite sensitive to the nature of the X substituent. It gains in intensity and is hypsochromically shifted when the para substituent becomes more and more electron-releasing (Figure 4). This substituent effect is opposite to the effect stated on the low-energy visible absorptions. The chloride and the hydride complexes (**2**[$PF_6$] and **3**[$PF_6$]) also present a similar absorption in the near-IR range near 1500 nm.[31] For all these Fe(III) radicals, the presence of these near-IR absorptions was confirmed in the solid state by means of diffuse scattering on powdered samples. Actually, the very weak extinction coefficient for this near-IR absorption is reminiscent of a forbidden metal-centered ligand field (LF) electronic transition. This hypothesis would also be in line with its apparently poor sensitivity to the solvent nature and with the fact that a similar low-energy absorption is observed for **2**[$PF_6$] and **3**[$PF_6$], which both lack the acetylide ligand. Notably, similar absorptions were previously observed in mono- and polynuclear Fe(III) acetylide complexes.[18,19] Theoretical computations were carried out in order to check these tentative statements.

**DFT Computations.** Theoretical computations on the Fe(III) model complexes **1a**-$H^+$ (X = $NO_2$), **1b**-$H^+$ (X = CN), **1d**-$H^+$ (X = Br), **1f**-$H^+$ (X = H), **1i**-$H^+$ (X = OMe), and **1j**-$H^+$ (X = $NH_2$), with the chelating dppe ligand replaced by two $PH_3$ ligands and $C_5Me_5$ replaced by $C_5H_5$, were previously performed.[5] They indicated that the electron is lost from a delocalized molecular orbital heavily weighted on the metal center in the Fe(II) parent molecules. The effect of oxidation on the energies of the molecular orbitals is depicted in Figure 5 for **1j** and **1j**-$H^+$ (X = $NH_2$) using a spin-restricted representation, to simplify the discussion. As can be seen in this diagram, the HOMO−LUMO gap slightly increases upon oxidation.

(28) Rieger, A. L.; Rieger, P. H. *Organometallics* **2004**, *2004*, 154−162.
(29) Connelly, N. G.; Kitchen, M. D. *J. Chem. Soc., Dalton Trans.* **1977**, 931−937.
(30) Belkova, N. V.; Revin, P. O.; Epstein, L. M.; Vorontsov, E. V.; Bakhmutov, V. I. *J. Am. Chem. Soc.* **2003**, *125*, 11106−11115.
(31) As precised above, a slow decomposition of **3**[$PF_6$] was observed in dichloromethane, evidenced by the progressive disappearance of the corresponding electronic absorptions. The spectra of this sensitive sample were therefore acquired several times with concentrated solutions and over short time scales to ascertain that the observed absorptions did indeed correspond to **3**[$PF_6$]. The reported extinction coefficients remain nevertheless approximate.

**Table 5. UV−Vis Data for [($\eta^2$-dppe)($\eta^5$-$C_5Me_5$)FeC≡CAr][$PF_6$] Complexes in $CH_2Cl_2$ Solution**

| Ar | abs (nm) ($10^{-3}\epsilon$ ($M^{-1}$ $cm^{-1}$)) | $\Delta\nu$ ($cm^{-1}$)[a] |
|---|---|---|
| Cl | 266 (sh, 16.3); 284 (sh, 16.8); 466 (2.4); 550 (sh, ca. 1.0) | |
| H | 302 (sh, 4.9); 382 (1.6); 536 (sh, 0.3) | |
| *p*-($C_6H_4$)$NO_2$ | 267 (sh, 85.4); 310 (sh, 16.1); 379 (15.4); 504 (sh, 2.3); 562 (sh, 1.6); 650 (1.2) | 2410 |
| *p*-($C_6H_4$)CN | 263 (sh, 40.5); 326 (sh, 12.5); 394 (sh, 2.8); 458 (sh 1.4); 501 (1.1); 564 (1.0); 652 (0.9) | 2390 |
| *p*-($C_6H_4$)$CF_3$ | 261 (sh, 44.9); 298 (sh, 26.0); 342 (sh, 5.2); 379 (sh, 2.7); 430 (sh 1.8); 515 (1.5); 557 (1.7); 635 (1.5) | 2210 |
| *p*-($C_6H_4$)Br | 356 (sh, 13.8); 391 (sh, 11.2); 579 (sh, 1.8); 670 (2.4) | 2350 |
| *p*-($C_6H_4$)F | 349 (sh, 5.6); 388 (sh, 3.1); 576 (2.4); 661 (3.4) | 2230 |
| *p*-($C_6H_5$) | 261 (sh, 32.6); 280 (sh, 27.4); 301 (sh, 18.8); 342 (sh, 5.9); 379 (sh, 3.6); 575 (sh, 2.3); 662 (3.1) | 2290 |
| *p*-($C_6H_4$)Me | 262 (40.7); 350 (sh, 5.6); 397 (sh, 2.9); 589 (sh, 2.1); 686 (4.2) | 2480 |
| *p*-($C_6H_4$)$^t$Bu | 259 (73.0); 299 (sh, 42.7); 344 (sh, 6.3); 395 (sh, 3.5); 584 (sh, 2.3); 683 (3.8) | 2480 |
| *p*-($C_6H_4$)OMe | 265 (46.2); 323 (sh, 10.0); 352 (6.5) 394 (sh, 3.6); 440 (sh, 1.5); 519 (1.3); 615 (1.9); 718 (6.1) | 2330[b] |
| *p*-($C_6H_4$)$NH_2$ | 268 (sh, 34.5); 287 (8.8); 413 (sh, 6.0); 595 (1.2); 789 (9.7) | 4130 |
| *p*-($C_6H_4$)$NMe_2$ | 263 (sh, ≥34.1); 278 (67.0); 414 (19.8); 894 (24.7) | |

[a] Energetic difference (±100 $cm^{-1}$) between the two low-energy transitions. [b] A significantly larger value (2760 $cm^{-1}$) was found by deconvolution of the peaks in this case.

**Table 6. Near-IR Data for [($\eta^2$-dppe)($\eta^5$-$C_5Me_5$)FeX][$PF_6$][a] Complexes**

| | soln[b] | | solid[c] | |
|---|---|---|---|---|
| X | $\nu_{max}$[d] ($\epsilon$[e]) | $\nu_{1/2}$[f] | $\nu_{max}$[d] | $\nu_{1/2}$[f] |
| Cl | 1572/6361 (11) | 1300 | 1610/6210 | 1400 |
| H | 1384/7225 (26) | 1900 | 1322/7560 | 1850 |
| C≡C($C_6H_4$)$NO_2$ | 1936/5165 (70) | 1500 | 1912/5230 | 1400 |
| C≡C($C_6H_4$)CN | 1916/5219 (75) | 1400 | 1908/5240 | 1400 |
| C≡C($C_6H_4$)$CF_3$ | 1900/5263 (68) | 1400 | 1894/5280 | 1400 |
| C≡C($C_6H_4$)F | 1824/5482 (93) | 1500 | 1818/5500 | 1400 |
| C≡C($C_6H_4$)Br | 1864/5364 (113) | 1500 | 1757/5691 | 1500 |
| C≡C($C_6H_4$) | 1846/5417 (94) | 1500 | 1865/5360 | 1400 |
| C≡C($C_6H_4$)Me | 1808/5531 (99) | 1600 | 1835/5450 | 1400 |
| C≡C($C_6H_4$)$^t$Bu | 1808/5531 (124) | 1700 | 1835/5450 | 1700 |
| C≡C($C_6H_4$)OMe | 1752/5707 (139) | 1900 | 1792/5580 | 1600 |
| C≡C($C_6H_4$)$NH_2$ | 1664/6203 (243) | 2300 | 1672/5980 | 2000 |
| C≡C($C_6H_4$)$NMe_2$[g] | 1588/6297 (427) | 2500 | 1588/6295 | 2000 |

[a] Unless precised; $\nu$ in nm/$cm^{-1}$ and $\epsilon$ in $M^{-1}$ $cm^{-1}$. [b] Conditions: $CH_2Cl_2$, absorbance mode, 20 °C (Cary 5). [c] Conditions: KBr, diffuse reflectance mode, 20 °C (Bruker IFS 28). [d] Values ±20 nm/±50 $cm^{-1}$. [e] Values ±5 $M^{-1}$ $cm^{-1}$. [f] Values ±200 $cm^{-1}$. [g] No changes upon dilution (×3) of the solution.

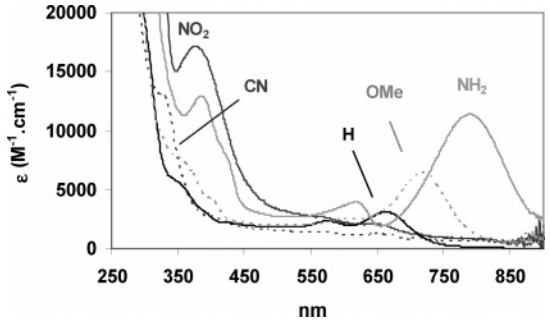


**Figure 3.** UV−vis spectra for selected Fe(III) complexes (X = $NO_2$, CN, H, OMe, $NH_2$) in dichloromethane.

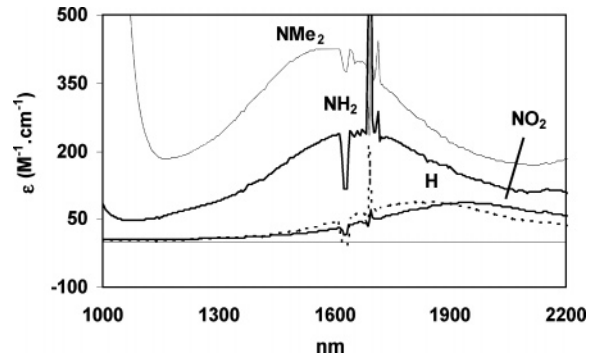


**Figure 4.** Near-IR spectra for selected Fe(III) complexes (X = $NO_2$, H, $NH_2$, $NMe_2$) in dichloromethane.

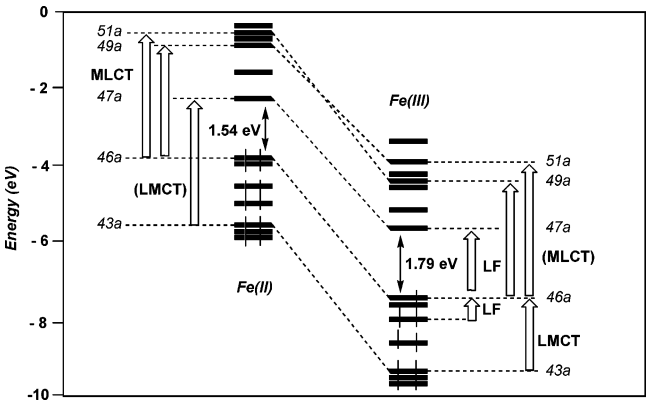


**Figure 5.** Orbital diagram for [$(H_3P)_2$($\eta^5$-$C_5H_5$)Fe(C≡C)-1,4-($C_6H_4$)$NH_2$]$^{0/+}$ (**1j**-H/**1j**-$H^+$) showing the effect of oxidation on the energy levels. The arrows indicate the possible excitations leading to MLCT, LMCT, or LF transitions in the visible range. Transitions in parentheses were not observed in the visible spectrum (400−800 nm).

The LUMO for these electron-rich compounds has a dominant $d_{xy}$ character, whereas the LUMO + 1 has a dominant $d_{z^2}$ character. As previously described, these MOs correspond to the $e_g$ set of an homoleptic octahedral complex, while the SOMO and the two MOs below correspond to the $t_{2g}$ set.[5] The SOMO and SOMO − 1 exhibit an important metal $d_{yz}$ or $d_{xz}$ character, as well as an important acetylide character (Table 7).[32]

Spin-unrestricted calculations were next carried out. The energies of the six frontier spin MOs (α and $\beta$) possessing a large metal character in **1a**-$H^+$−**1j**-$H^+$ (two are unoccupied and four are occupied) are shown in Figure 6. Except for **1f**-$H^+$, the metal contribution of the higher lying spin MOs among these is dominated by one type of d atomic orbital (Table 7). In contrast, the metal contribution of the lower lying spin MOs is more accurately described by a mixture of two d AOs. Notably, in the case of complex **1a**-$H^+$, the filled spin MOs are interspersed by three aryl- and nitro-based MOs (not represented in Figure 6).

For all compounds, the highest occupied α-spin MO has a dominant $d_{yz}$ character. This is not the case for the lowest empty $\beta$-spin MOs. Actually, depending on the X substituent in **1a**-$H^+$−**1f**-$H^+$, different trends are

(32) Lichtenberger, D. L.; Renshaw, S. K.; Bullock, R. M. *J. Am. Chem. Soc.* **1993**, *115*, 3276−3285.

**Table 7. Decomposition of $(PH_3)_2(\eta^5\text{-}C_5H_5)Fe(C{\equiv}CC_6H_4X)$ Model Complexes (X = $NO_2$, H, $NH_2$) for Selected Frontier MOs**

| | **1a**-$H^+$ (X = $NO_2$) | | | | | | | | | | | |
|---|---|---|---|---|---|---|---|---|---|---|---|---|
| | MO | | | | | | | | | | | |
| | 53a(α) | 53a(β) | 52a(α) | 52a(β) | 51a(α) | 51a(β) | 48a(α) | 50a(β) | 46a(α) | 46a(β) | 44a(α) | 44a(β) |
| ϵ (eV) | −6.59 | −6.30 | −7.19 | −6.87 | −8.62 | −8.29 | −9.39 | −8.47 | −9.73 | −9.44 | −10.01 | −9.77 |
| occ | 0 | 0 | 0 | 0 | 1 | 0 | 1 | 1 | 1 | 1 | 1 | 1 |
| % Fe | 48 | 53 | 46 | 51 | 18 | 56 | 37 | 27 | 75 | 79 | 54 | 48 |
| % Cp | 14 | 19 | 18 | 24 | 0 | 5 | 4 | 8 | 11 | 1 | 0 | 0 |
| % P | 7 | 6 | 20 | 19 | 0 | 0 | 0 | 2 | 0 | 2 | 0 | 0 |
| % $C_\alpha$ | 11 | 10 | 0 | 0 | 18 | 7 | 12 | 16 | 0 | 0 | 1 | 5 |
| % $C_\beta$ | 1 | 1 | 0 | 0 | 17 | 21 | 28 | 16 | 0 | 0 | 3 | 0 |
| % C(Ph) | 3 | 0 | 0 | 0 | 36 | 0 | 0 | 28 | 0 | 0 | 28 | 32 |
| % $NO_2$ | 2 | 0 | 0 | 0 | 3 | 0 | 0 | 3 | 0 | 0 | 2 | 2 |
| | **1f**-$H^+$ (X = H) | | | | | | | | | | | |
| | MO | | | | | | | | | | | |
| | 45a(α) | 45a(β) | 44a(α) | 44a(β) | 43a(α) | 43a(β) | 42a(α) | 42a(β) | 41a(α) | 41a(β) | 39a(α) | 39a(β) |
| ϵ (eV) | −5.94 | −5.71 | −6.53 | −6.29 | −8.22 | −7.83 | −8.60 | −8.01 | −9.02 | −8.73 | −9.62 | −9.24 |
| occ | 0 | 0 | 0 | 0 | 1 | 0 | 1 | 1 | 1 | 1 | 1 | 1 |
| % Fe | 50 | 52 | 46 | 51 | 29 | 45 | 37 | 43 | 76 | 74 | 55 | 50 |
| % Cp | 20 | 18 | 26 | 23 | 1 | 3 | 4 | 2 | 6 | 7 | 0 | 0 |
| % P | 8 | 9 | 20 | 18 | 0 | 0 | 1 | 0 | 2 | 2 | 0 | 0 |
| % $C_\alpha$ | 10 | 10 | 0 | 0 | 15 | 10 | 9 | 10 | 0 | 0 | 5 | 7 |
| % $C_\beta$ | 1 | 1 | 0 | 0 | 18 | 19 | 21 | 20 | 0 | 0 | 4 | 0 |
| % C(Ph) | 0 | 0 | 0 | 0 | 26 | 15 | 13 | 14 | 0 | 0 | 21 | 32 |
| | **1j**-$H^+$ (X = $NH_2$) | | | | | | | | | | | |
| | MO | | | | | | | | | | | |
| | 48a(α) | 48a(β) | 47a(α) | 47a(β) | 46a(α) | 46a(β) | 45a(α) | 45a(β) | 44a(α) | 44a(β) | 43a(α) | 43a(β) |
| ϵ (eV) | −5.30 | −5.17 | −5.83 | −5.65 | −7.69 | −7.21 | −7.72 | −7.54 | −8.20 | −7.93 | −8.87 | −8.44 |
| occ | 0 | 0 | 0 | 0 | 1 | 0 | 1 | 1 | 1 | 1 | 1 | 1 |
| % Fe | 49 | 51 | 49 | 53 | 17 | 29 | 56 | 58 | 76 | 66 | 53 | 52 |
| % Cp | 19 | 19 | 25 | 19 | 0 | 0 | 5 | 5 | 5 | 7 | 0 | 0 |
| % P | 7 | 8 | 19 | 18 | 0 | 0 | 0 | 0 | 2 | 0 | 0 | 0 |
| % $C_\alpha$ | 11 | 11 | 0 | 0 | 16 | 12 | 6 | 5 | 0 | 2 | 0 | 2 |
| % $C_\beta$ | 1 | 1 | 0 | 0 | 10 | 13 | 23 | 22 | 0 | 0 | 0 | 3 |
| % C(Ph) | 0 | 0 | 0 | 0 | 37 | 28 | 0 | 0 | 0 | 2 | 24 | 20 |
| % $NH_2$ | 0 | 0 | 0 | 0 | 13 | 10 | 0 | 0 | 0 | 2 | 12 | 12 |

observed for the energies of the frontier α-spin and β-spin MOs containing the unpaired electron. Thus, starting from **1f**-$H^+$, the α-spin filled $\pi_y$ and $\pi_x$ MOs separate in energy when the substituent becomes more and more electron withdrawing, while the corresponding β-spin $\pi_y$ and $\pi_x$ MOs become closer in energy and eventually cross for X = $NO_2$. This is in fact an avoided crossing, since admixture between these spin MOs is allowed under $C_1$ symmetry. Actually, admixture clearly happens in **1f**-$H^+$ (X = H), where the two filled frontier α-spin MOs (Figure 7) extend over both the $\pi_y$ and $\pi_x$ manifold on the acetylide linker. The admixture between the two occupied frontier α-spin MOs has quite important consequences for the unpaired spin distribution, as discussed below, and illustrates the decisive X-substituent influence on the SOMO in these compounds.

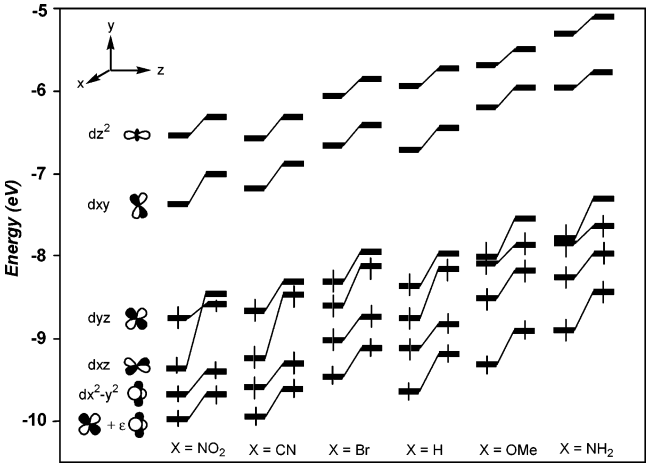


**Figure 6.** Energy of the frontier molecular spin orbitals of the $[(H_3P)_2(\eta^5\text{-}C_5H_5)Fe(C{\equiv}C)\text{-}1,4\text{-}(C_6H_4)X]^+$ (**1a**-$H^+$−**1j**-$H^+$) model complexes (X = $NO_2$, CN, Br, H, OMe, $NH_2$), presenting a strong metallic character. The dominant metal-centered AOs are represented on the left.

The spin distribution computed for **1a**-$H^+$−**1j**-$H^+$ is given in Table 8. The largest positive spin density is computed on the metal and then on the β-carbon atom of the acetylide. It is strongly influenced by the X substituent, being larger on these atoms for the most electron-withdrawing substituents. The spin delocalization on the aryl acetylide is clearly favored for the most electron-releasing substituents, spreading more and more on the aryl ring. As a result of the avoided crossing mentioned above, the unpaired spin density is located in the π manifold conjugated with the aryl ring for the compounds bearing the electron-releasing substituents and in the perpendicular π manifold for the electron-accepting X substituents, while for compounds with a moderate substituent such as **1f**-$H^+$, the spin density is located around the acetylide bridge, in both $\pi_x$ and $\pi_y$ manifolds. This shows that the spatial location of the unpaired spin density in the arylacetylide is

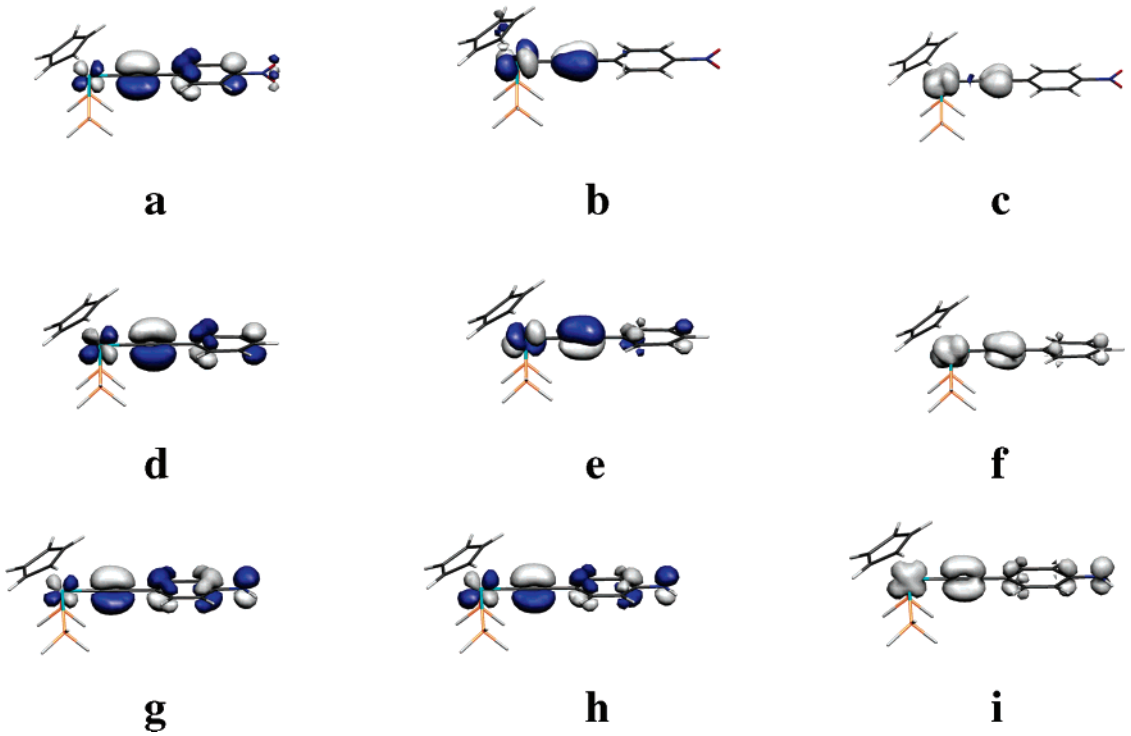


**Figure 7.** Plots of the highest occupied spin MO (left), of the lowest unoccupied spin MO (center) and of the total spin density (right) of $(H_3P)_2(\eta^5\text{-}C_5H_5)Fe(C{\equiv}C)\text{-}1,4\text{-}(C_6H_4)X$ complexes: (a−c) X = $NO_2$; (d−f) X = H; (g−i) X = $NH_2$. The contour values are 0.05 [e/bohr$^3$]$^{1/3}$.

**Table 8. Calculated Unpaired Spin Densities for $[(PH_3)_2(\eta^5\text{-}C_5H_5)Fe(C{\equiv}CC_6H_4X)]^+$ Complexes (X = $NO_2$, CN, Br, H, OMe, $NH_2$)**

| | **1a**-H$^+$ (X = $NO_2$) | **1b**-H$^+$ (X = CN) | **1d**-H$^+$ (X = Br) | **1f**-H$^+$ (X = H) | **1i**-H$^+$ (X = OMe) | **1j**-H$^+$ (X = $NH_2$) |
|---|---|---|---|---|---|---|
| Fe | 0.799 | 0.734 | 0.598 | 0.637 | 0.508 | 0.427 |
| $C_\alpha$ | −0.054 | −0.020 | 0.047 | 0.042 | 0.108 | 0.134 |
| $C_\beta$ | 0.306 | 0.266 | 0.209 | 0.241 | 0.147 | 0.133 |
| $C_6H_4X$ | 0.012 | 0.079 | 0.210 | 0.151 | 0.315 | 0.382 |
| $C_5H_5$ | −0.036 | −0.035 | −0.036 | −0.037 | −0.041 | −0.039 |
| $2PH_3$ | −0.027 | −0.024 | −0.028 | −0.034 | −0.037 | −0.037 |

strongly modulated by the substituent. The positive values found for the unpaired spin density on the arylacetylide ligand suggest that the spin density is mostly delocalized by Fermi contact. Comparatively, the spin delocalization in the $\eta^5$-$C_5H_5$ and phosphane ligands is lower and overall negative, suggesting that spin polarization mechanisms are also operative there.

In the absence of TD-DFT calculations, the discussion of the electronic transitions of **1a**$^+$−**1k**$^+$ has to be based on the ground-state energy diagrams established for **1a**-H$^+$−**1j**-H$^+$. Such an approach is at best qualitative, since no account is given to electronic relaxation in the excited state.[33] Accordingly, assignment of the lowest energy (near-IR) transitions proves rather problematic using these diagrams. Nevertheless, some general statements can be made. The SOMO−LUMO gap computed for the α-spin MOs in all complexes being much larger than the energies of the low-energy electronic transitions experimentally measured, these must involve the promotion of an electron from lower lying MOs in the SOMO (no transition is strictly symmetry forbidden in such compounds under $C_1$ point-group symmetry). Thus, the observed near-IR transition must correspond either to the SOMO − 1/SOMO or to the SOMO − 2/SOMO transition. Actually, the energy difference between SOMO and SOMO − 1 levels of the β-spin orbitals increases as the X substituent becomes more and more electron releasing (Figure 6), in line with the observed substituent effect on the near-IR absorption. However, the energy gaps do not match with the energies of the near-IR transitions of **1a**$^+$−**1j**$^+$, being roughly one-fourth to one-third of the energies experimentally found. The energy gaps between the SOMO and the next metal-centered MOs which possess a strong $d_{x^2-y^2}$ character (Figure 6) are actually much closer but are calculated to follow a reverse energetic trend depending on the substituent. However, further evidence for the latter assignment comes from the ESR data (see Discussion).

Comparison between MOs derived for **1a**-H$^+$−**1j**-H$^+$ and **1a**-H−**1j**-H indicate that the MLCT transitions computed for Fe(II) parents should be shifted toward higher energies in the corresponding Fe(III) complexes and might, therefore, no longer be detected above 300 nm for most compounds (Figure 5). Conversely, several LMCT transitions, previously very energetic in Fe(II) complexes, are shifted to lower energies and might now become observable with Fe(III) complexes, since several occupied levels with a dominant acetylide or phenyl character are located 2.1−2.3 eV below the SOMO. These levels (or some of lower energy) could typically give rise to a LMCT transition that would appear in the visible range (Figure 5). Alternatively, the low-energy transitions observed in the visible range could also

(33) (a) Powell, C. E.; Cifuentes, M. P.; Morall, J. P.; Stranger, R.; Humphrey, M. G.; Samoc, M.; Luther-Davies, B.; Heath, G. A. *J. Am. Chem. Soc.* **2003**, *125*, 602−610. (b) Morrall, J. P.; Powell, C. E.; Stranger, R.; Cifuentes, M. P.; Humphrey, M. G.; Heath, G. A. *J. Organomet. Chem.* **2003**, *670*, 248−255.

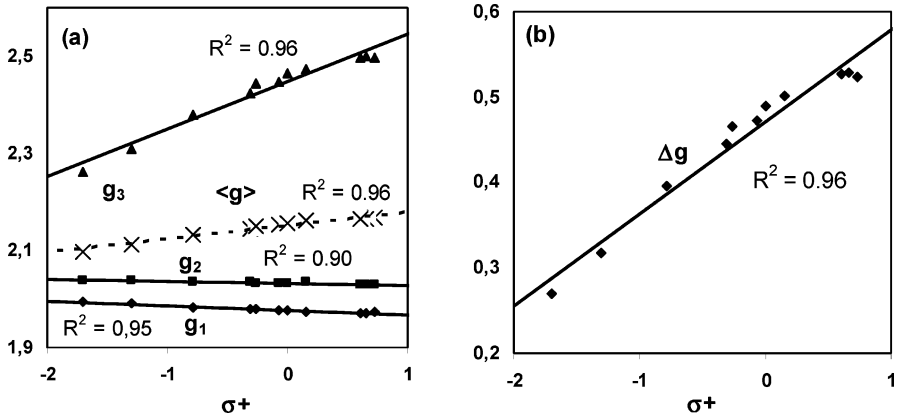


**Figure 8.** Plots of the (a) ESR principal and mean $g$ values and (b) **g** tensor anisotropy vs $\sigma^+$ ESPs for [($\eta^2$-dppe)($\eta^5$-$C_5Me_5$)Fe(C≡C)-1,4-($C_6H_4$)X][$PF_6$] complexes (X = $NO_2$, CN, $CF_3$, F, Br, H, Me, $^t$Bu, OMe, $NH_2$, $NMe_2$).

correspond to transitions between the SOMO and the LUMO or LUMO + 1. However, according to Laporte's rule,[34] these transitions are expected to show up less intensely than the (symmetry allowed) LMCT mentioned above, since they take place between MOs possessing a strong metal d character.

**ESP Correlations with ESR or UV−Vis/Near-IR Spectrochemical Data.** Significant linear correlations have previously been reported between electronic substituent parameters (ESP) and infrared data for these Fe(III) complexes. We have checked here if similar correlations could also be obtained with characteristic ESR or spectral data. The three lowest electronic absorptions observed for these compounds as well as the various **g** tensors recorded by ESR give significant linear correlations ($R^2$ > 0.95) when plotted against the Hammett or $\sigma^+$ ESP sets (see the Supporting Information). The correlations with ESR data are shown in Figure 8. Notably, a good linear correlation is also obtained with the **g** tensor anisotropy ($\Delta g$). As previously stated with infrared data,[2] better results were obtained with the $\sigma^+$ parameters than with the regular Hammett $\sigma_p$ set for single ESP correlations. This clearly evidences an electronic substituent effect with a dominant mesomeric contribution. Following the method of Jiang,[35] we next checked if some improvements in the fits could be obtained when an ESP set reflects the spin delocalization properties of the substituent, such as $\sigma_{JJ}$ for instance. However, no linear correlations at all were found with this set alone, while only slight improvements on the fits were stated in dual correlations including $\sigma_{JJ}$ and an additional ESP set reflecting the polar character of the substituent (such as $\sigma^+$). Thus, substituent-centered spin-delocalization effects are apparently not determining regarding this electronic effect of the X substituent on the ESR and UV−vis−near-IR data.

## Discussion

In accordance with previous data on closely related complexes,[10,14,21,36] Evans measurements confirm that the functionalized arylacetylide Fe(III) complexes **1a**[$PF_6$]−**1j**[$PF_6$] are low-spin radical cations possessing one unpaired electron ($S$ = $^1/_2$). Despite the small structural changes evidenced by X-ray studies, DFT calculations indicate that sizable spin delocalization takes place within the arylacetylide ligand (Table 8).[5] Indeed, the quite large spin density computed on the $\beta$-carbon is in line with a recent study on the reactivity of these compounds with dioxygen.[24] As expected for such piano-stool $d^5$ radicals, rhombic ESR spectra were obtained for all of them, with three principal **g** tensor values in the order $g_{min} < g_e \leq g_{int} < g_{max}$.[14] As is often observed for Fe(III)-centered radicals, the spin relaxation of these species is too fast to allow for the detection of the hyperfine structure.[10] The ESR signal is usually very sensitive to the symmetry of the SOMO and to its energy separation from the other metal-based frontier MOs in these organometallic radicals.[37] To rationalize the experimental data obtained for **1a**[$PF_6$]−**1j**[$PF_6$], the ESR **g** tensor values were derived from the frontier MOs calculated for **1a**-$H^+$−**1j**-$H^+$.

**Frontier MOs of 1a-$H^+$−1j$^+$-H and g Tensor Anisotropy in 1a[$PF_6$]−1j[$PF_6$].** In complexes **1a**-$H^+$−**1j**$^+$-H, the $\sigma$ and $\pi$ MOs of the acetylide fragment overlap significantly with the $t_{2g}$ d AOs of the metal center.[5] As discussed above, this has a strong influence on the metal d composition and the energy ordering of the frontier MOs.[38] These parameters are determinant for the ESR $g$ anisotropy. Notably, our data differ somewhat from those of previous EHMO calculations on related $d^5$ piano-stool radicals containing electron poorer ligands, such as CO in place of $PH_3$,[39] or R ligands without $\pi$ orbitals.[21] Our calculations compare better with recent DFT computations reported for Ru(III) analogues by Rousseau et al.[40] They show that, depending on the X substituent, the SOMO location in these Fe(III) compounds changes. Thus, it extends mainly on the acetylide bridge and to a lesser extent on the $\pi$ manifold of the functional aryl group for

(34) Atkins, P. W. *Physical Chemistry*, 6th ed.; Oxford University Press: Oxford, U.K., 1998; p 501.
(35) Jiang, X.-K. *Acc. Chem. Res.* **1997**, *30*, 283−289.
(36) Morrow, J.; Catheline, D.; Debois, M.-H.; Manriquez, J.-M.; Ruiz, J.; Astruc, D. *Organometallics* **1987**, *6*, 2605−2607.
(37) Rieger, P. H. *Coord. Chem. Rev.* **1994**, *135/136*, 203−286.
(38) Powell, C. E.; Cifuentes, M. P.; MacDonagh, A.; Hurst, S. K.; Lucas, N. T.; Delfs, C. A.; Stranger, R.; Humphrey, M. G.; Houbrechts, S.; Asselberghs, I.; Persoons, A.; Hockless, D. C. *Inorg. Chim. Acta* **2003**, *352*, 9−18.
(39) (a) Schilling, B. E. R.; Hoffmann, R.; Lichtenberger, D. L. *J. Am. Chem. Soc.* **1979**, *101*, 585−591. (b) Kostic, N. M.; Fenske, R. F. *Organometallics* **1982**, *1*, 974−982. (c) Sponsler, M. B. *Organometallics* **1995**, *14*, 1920−1927.
(40) Koentjoro, O. F.; Rousseau, R.; Low, P. J. *Organometallics* **2001**, *20*, 4502−4509.

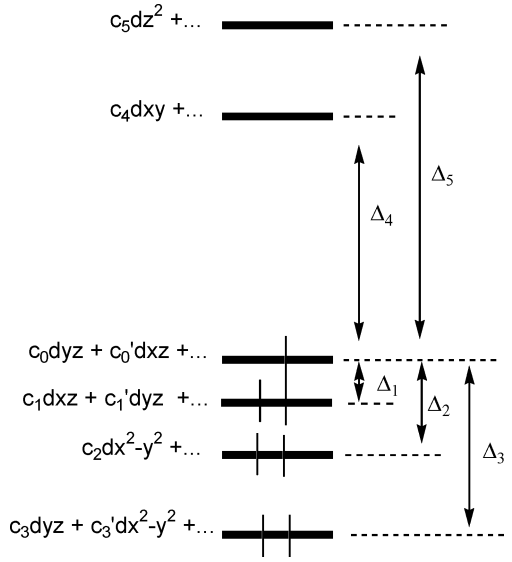


**Figure 9.** Schematic spin-restricted representation of the frontier MOs for $d^5$ piano-stool radicals such as $[(PH_3)_2(\eta^5\text{-}C_5H_5)Fe(C{\equiv}CC_6H_4X)]^+$ with $C_1$ symmetry.

compounds with electron-releasing substituents. The SOMO presents a dominant $d_{yz}$ metal character in these complexes, while the SOMO − 1 is mostly $d_{xz}$ and the LUMO mostly $d_{xy}$ in character (Figure 7).[18,41] For unsubstituted complexes, the SOMO is a mixture of $d_{yz}$ and $d_{xz}$ and becomes purely $d_{xz}$ with electron-withdrawing groups (Figure 7).

The atomic composition given in Figure 9 has therefore been considered for the five frontier MOs presenting a large metallic contribution (Figure 6), using a spin-restricted formalism, and the various $g_{ii}$ components of the tensor have been derived using a perturbative approach to the first order (eq 1).[28] Several classic

$$g_{ij} = g_e\delta_{ij} + 2\zeta\sum_{m\neq 0}(\langle 0|\hat{I}_i|m\rangle\langle m|\hat{I}_j|0\rangle)/(E_0 - E_m) \quad (1)$$

simplifying assumptions have been made to obtain this expression.[42] Notably, the influence of spin−orbit coupling from the carbon atoms of the arylacetylene ligand has been neglected.[43]

The expressions of the $g_{ii}$ values are quite complicated in the general case (Supporting Information), but an important simplification takes place in the case of electron-releasing substituents (eqs 2−4), since the **g** tensor becomes diagonal in the referential chosen. In

$$g_{xx} = g_e + 2\zeta(c_0c_2)^2/(\Delta_2) - 6\zeta(c_0c_5)^2/(\Delta_5) + 2\zeta(c_0c_3')^2/(\Delta_3) \quad (2)$$

$$g_{yy} = g_e - 2\zeta(c_0c_4)^2/(\Delta_4) \quad (3)$$

$$g_{zz} = g_e + 2\zeta(c_0c_1)^2/(\Delta_1) \quad (4)$$

these equations, $g_e$ stands for the free electron $g$ value, $c_n$ values are the coefficients of the d AOs in the frontier MOs, according to Figure 9, and $\Delta_n$ values are the corresponding transition energies.

**Chart 3**

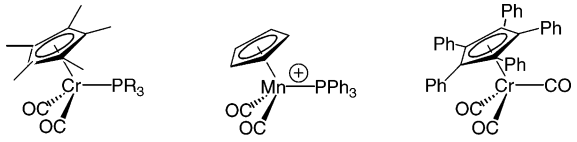


**5** **6**$^+$ **7**

In all cases, $g_{zz}$ corresponds to $g_3$ in the experimental ESR data obtained for **1a**$[PF_6]$−**1j**$[PF_6]$ ($g_1 < g_e \leq g_2 < g_3$). The main component of the magnetic anisotropy ($g_3$) is therefore along the $z$ direction with electron-releasing substituents and becomes somewhat tilted in the $yz$ plane for electron-withdrawing substituents. The $g$ anisotropy in **1a**$[PF_6]$−**1j**$[PF_6]$ is therefore different from that of related Cr(I) and Mn(II) piano-stool $d^5$ radicals of $C_s$ symmetry previously studied, such as **5** and **6** (Chart 3), for which the main component of the **g** tensor was found to be along the cyclopentadienyl centroid, somewhat tilted toward the most electron-rich ligand among the piano stool "legs".[16,17]

It is clear from the $g_{ii}$ values found in the general case that a single d−d transition cannot determine $g_1$ or $g_2$. Accordingly, very poor linear fits ($R^2 < 0.76$) are obtained between $g_2$ and the wavelength of all low-energy absorptions. In contrast, fairly linear correlations can be found ($R^2 = 0.92$) between the wavelength of the second band in the visible spectrum and $g_1$ (Supporting Information). Significant linear correlations are also found between $g_3$ or $g_1$ and the wavelength of the near-IR transition (Supporting Information). However, the near-IR transition is too energetic to be the SOMO − 1/SOMO transition ($\Delta_1$) (see below) and is not energetic enough to be $\Delta_4$, according to our calculations. Thus, these "unexpected" correlations evidence that these **g** tensor components and the corresponding electronic transitions experience a similar electronic substituent effect, rather than expressing any dependence through equations such as (1).

If, as assumed here, ESR anisotropy arises essentially from spin−orbit coupling, the more the unpaired electron is ligand-centered, the less anisotropic the ESR signal will be, its $g_{iso}$ value becoming concomitantly closer and closer to the $g_e$ value ($g_e = 2.0023$). Accordingly, the $g$ values for a free $\sigma$ radical obtained from phenylacetylene (PhC≡C•)[44] or for a related $\pi$ radical anion[45] are quite close to $g_e$. On the basis of this simple reasoning, we had previously proposed that the anisotropy of the ESR signal in dinuclear mixed-valence complexes was related to the "metal vs bridge" character of the unpaired electron.[46] In this work, our calculations on **1a**-H$^+$−**1k**-H$^+$ confirm that the anisotropy decreases with the decrease of the total spin density on the iron atom and the Hirschfeld charge on the metal center. However, no strict linear dependence can be evidenced between $\Delta g$ and these quantities (Figure 10). In line with this statement, the asymmetry recorded for the chloride and hydride Fe(III) complexes, **2**$[PF_6]$ and **3**$[PF_6]$ (ca. 0.450), compares to that obtained for **1h**$[PF_6]$

(41) Weyland, T.; Lapinte, C.; Frapper, G.; Calhorda, M. J.; Halet, J.-F.; Toupet, L. *Organometallics* **1997**, *16*, 2024−2031.
(42) Stone, A. J. *Proc. R. Soc. (London), Ser. A* **1963**, *271*, 424−434.
(43) Neese, F.; Solomon, E. I. *Inorg. Chem.* **1998**, *37*, 6568−6582.
(44) Coleman, J. S.; Hudson, A.; Root, K. D. J.; Walton, D. R. M. *Chem. Phys. Lett.* **1971**, *11*, 300−301.
(45) Evans, A. G.; Evans, J. C.; Phelan, T. J. *J. Chem. Soc., Perkin Trans. 2* **1974**, 1216−1219.
(46) Le Stang, S.; Paul, F.; Lapinte, C. *Organometallics* **2000**, *19*, 1035−1043.

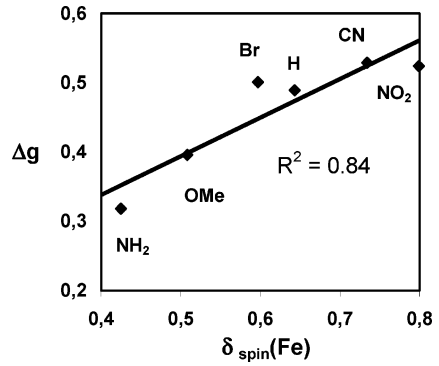


**Figure 10.** Plot of the of the ESR **g** tensor anisotropy for $[(\eta^2\text{-dppe})(\eta^5\text{-}C_5Me_5)Fe(C{\equiv}C)\text{-}1,4\text{-}(C_6H_4)X][PF_6]$ complexes vs spin density computed for $[(PH_3)_2(\eta^5\text{-}C_5H_5)Fe(C{\equiv}C)\text{-}1,4\text{-}(C_6H_4)X]^+$ model complexes (X = $NO_2$, CN, Br, H, OMe, $NH_2$).

**Chart 4**

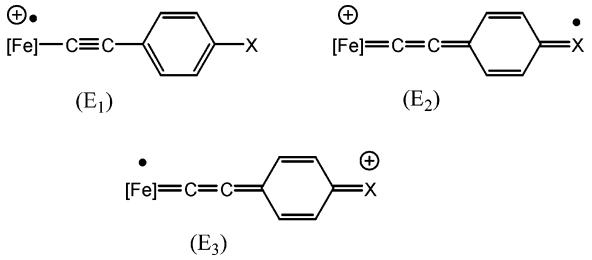


bearing the 4-*tert*-butyl-1-phenylacetylene ligand, whereas computations suggest a far more pronounced metallic character for the SOMOs in the latter compounds, as well as a larger unpaired spin and charge densities at the metal center, than for **1h**$[PF_6]$.[23a] This discrepancy possibly partly originates from the different nature of the frontier MOs in these compounds featuring a R ligand less $\pi$ bonding than arylacetylides. These complexes might also present a slightly different anisotropy of the **g** tensor.[21] We therefore want to stress here that the anisotropy of the rhombic ESR signal for $[(\eta^2\text{-dppe})(\eta^5\text{-}C_5Me_5)FeR][PF_6]$ radicals can be used to derive the relative metallic character of the SOMOs *only for complexes with structurally close R groups* (i.e. arylacetylide complexes).

**Electronic Transitions.** LF transitions such as $\Delta_1$–$\Delta_3$ (Figure 9) constitute the lowest energy transitions in these complexes. Such forbidden transitions will not induce large changes in the bonding within the Fe–C≡C core in the excited state and might therefore not be detected experimentally (Laporte's rule). MO diagrams suggest that the excited states in these transitions are in agreement with the valence-bond (VB) structure $E_1$ (Chart 4).

Among these LF transitions, the SOMO − 1/SOMO transition ($\Delta_1$) is particularly important since it determines the strongest diagonal **g** tensor component (eq 4). DFT computations indicate that this electronic transition corresponds to the promotion of one electron delocalized in the $\pi_x$ manifold of this fragment into the perpendicular $\pi_y$ manifold (Figure 6), except for **1a**-$H^+$, in which the reverse transition takes place. From the expression of $g_{zz}$ established above (eq 4) and from the experimental values ($g_3$) determined for **1a**$[PF_6]$–**1k**$[PF_6]$, one can derive the magnitude of the SOMO − 1/SOMO transition ($\Delta_1$). Obviously, the transition detected in the near-IR range (Table 6) *cannot* correspond to the SOMO − 1/SOMO transition ($\Delta_1$). Indeed, considering a maximum value for the spin–orbit coupling of a $d^5$ Fe(III) ion ($\zeta = 460$ cm$^{-1}$)[47] and considering $c_0 = c_1 = 1$ in eq 4, maximum values can be derived for $\Delta_1$ (1940–3400 cm$^{-1}$), which remain far below the energies of the transition detected in the near-IR domain for each compound. Most probably, the observed near-IR transition does correspond to the SOMO − 2/SOMO transition ($\Delta_2$). As experimentally stated, its transition moment is expected to increase for the most electron-releasing substituents, in line with an increasing MLCT character imparted to this LF transition. Indeed, the SOMO becomes slightly more delocalized on the arylacetylide ligand for electron-releasing substituents, while the SOMO − 2 remains largely localized on the iron center. In related $d^5$ piano-stool radicals of $C_s$ symmetry such as $[CpMn(CO)_2(PPh_3)]^+$ (**6**$^+$) and $(C_5Ph_5)Cr(CO)_3$ (**7**) (Chart 3), presenting similar symmetry representations for the two occupied upper frontier MOs,[16] the SOMO − 1/SOMO transition also determines the strongest contribution to the **g** tensor for these organometallic radicals and could be detected at 5710 cm$^{-1}$ ($\epsilon$ ca. 100 cm$^{-2}$ M) and near 4000 cm$^{-1}$ ($\epsilon$ ca. 62 cm$^{-2}$ M) for **6**$^+$ and **7**, respectively.[48] This result led to the proposal that the increase of the largest $g$ value for isoelectronic radicals which varies in the sequence Fe(III) > Mn(II) > Cr(I) was a consequence of the diminished energetic separation between the $^2A'$ and $^2A''$ states, itself mostly determined by the SOMO/SOMO − 1 gap.[14] Despite the different expression previously found for $g_{zz}$ with **6**$^+$ and **7**, our present work confirms this proposal. However, the near-IR absorption detected now with **1a**$^+$–**1k**$^+$ corresponds to the SOMO − 2/SOMO transition, rather than to the SOMO − 1/SOMO transition.

Transitions from lower lying MOs dominantly localized on the acetylide bridge will be higher in energy (Figure 5). Notably, most of these MOs still possess a weak contribution of d AOs and cannot therefore be considered as pure LMCT transitions, although we will call them LMCT in the following. They should appear in the same energy range as LF transitions between the SOMO and the LUMO or the LUMO + 1, such as $\Delta_4$–$\Delta_5$ (Figure 9), but should have much larger transition moments. These LMCT transitions certainly correspond to the most intense transition(s) detected in the low-energy part of the visible range (650–900 nm), whereas $\Delta_4$ or $\Delta_5$, if detected, could be the weaker absorption detected at slightly higher energies. Similar LMCT assignments have previously been proposed for the low-energy transitions at the near-IR/visible edge in the complexes $[Ru(16\text{-}TMC)(C{\equiv}CC_6H_4X\text{-}p)_2]^+$ (**8**$^+$) and $[Ru(Me_2bipy)(PPh_3)_2Cl(C{\equiv}CR)]^+$ (**9**$^+$) (Chart 5).[8,33,49] However, for these compounds, the weak shoulder on the high-energy side of this absorption was attributed to a vibronic progression involving the acetylide stretch, the difference between respective maxima being typically below 1800 cm$^{-1}$.[8,49,50] Presently, the energetic differences ($\Delta E$) between the two low-energy absorptions in the visible range are around 2300 cm$^{-1}$ for **1a**$[PF_6]$–

(47) Dunn, T. M. *Trans. Faraday Soc.* **1961**, *57*, 1441–1444.
(48) Atwood, C. G.; Geiger, W. E. *J. Am. Chem. Soc.* **1994**, *116*, 10849–10850.
(49) Choi, M.-Y.; Chan, M. C.-W.; Zhang, S.; Cheug, K.-K.; Che, C.-M.; Wong, K.-Y. *Organometallics* **1999**, *2074*, 4–2080.

**Chart 5**

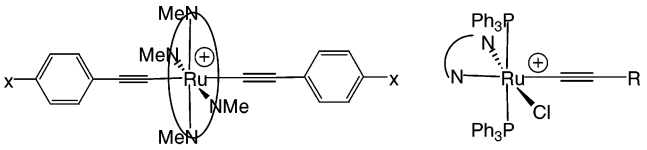


(X = OMe, Me, H, F, Cl) (R = $^t$Bu, Tol, Ph)

$8^+$ $9^+$

**Scheme 2**

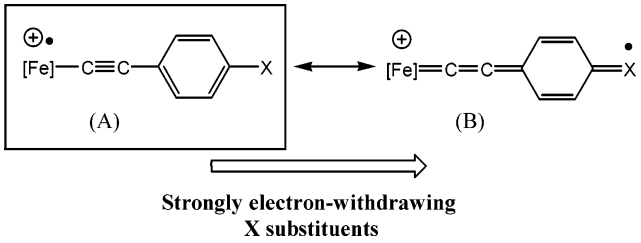


**1h**[$PF_6$] (Table 5). These differences are too large to correspond to a similar vibronic progression, and we tentatively suggest that the weak absorption near 16 670 $cm^{-1}$ (600 nm) corresponds to the SOMO/LUMO (LF) transition $\Delta_4$ (Figure 9). Notably, both LMCT and LF transitions experience a related substituent-induced shift. The substituent effect on their intensity is also in accordance with the composition of the frontier MOs discussed above, since the partial localization of the SOMO on the substituent imparts a slight LMCT character to $\Delta_4$ or $\Delta_5$, in contrast to the MLCT character imparted to $\Delta_1-\Delta_3$.

Whereas the VB description ($E_1$) can also be used to represent excited states resulting from LF transitions $\Delta_4-\Delta_5$, the VB representation $E_2$ (Chart 4) should be used to depict the LMCT excited state. In this VB structure, the metal is formally in the reduced Fe(II) oxidation state and presents a decreased acetylide bond order in the excited state, in accord with the depopulation of the acetylide $\pi$ (bonding) levels.[8,49] $E_2$ therefore constitutes a better representation of the MLCT state than $E_3$, previously proposed,[1−3] in which the metal center was formally in an Fe(I) oxidation state (19-electron metal center).

**Hyperpolarizabilities and VB Schemes.** NLO hyperpolarizabilities of several of these Fe(III) complexes were previously measured by EFISH.[3] The lowest energy excited states are usually determinant for this electronic property.[51] A few words are needed here, since we have previously overlooked the existence of the near-IR absorption while EFISH measurements were recorded under near-resonant conditions relative to this transition for several Fe(III) complexes. The simple two-level model used to rationalize the NLO data was therefore not fully appropriate, and a perturbational approach involving more excited states should have been considered to rationalize the static hyperpolarizabilities ($\beta_0$) for these Fe(III) compounds. Indeed, the existence of low-lying (near-IR) LF excited states helps in understanding the relatively weak hyperpolarizabilities (in absolute magnitude) observed for these Fe(III) complexes in comparison to those for the Fe(II) parents. However, considering the weak transition moments of these transitions along with the fact that they probably do not induce a large charge transfer along the metal−acetylide axis (see $E_1$ in Chart 4), our former VB interpretation of the NLO properties based on a single low-lying LMCT absorption in the visible range (such as $E_2$ or $E_3$) remains qualitatively correct, especially regarding the most electron-releasing substituents. The negative sign previously found for most $\beta$ values confirms that the GS of these Fe(III) complexes is admixed with excited states having diminished dipole moments along the acetylide axis in comparison to the GS under the influence of the laser light beam. As briefly discussed by Humphrey and co-workers,[33] low-lying (near-IR) transitions might have a much more profound effect on third-order NLO properties of these compounds.

**Electronic Substituent Effects.** The linear correlations obtained between the ESR data and $\sigma^+$ ESPs confirm the existence of electronic substituent effects, with a strong "mesomeric" character, transmitted from the aryl ring to the metal center through the alkynyl spacer. The failure to improve the linear fits by use of ESP sets tailored to analyze substituent-centered spin-delocalization effects suggests that the substituent influence in these Fe(III) complexes originates mostly from polarity changes induced by the X substituent. In accordance with related correlations on infrared data,[2] the substituent influence in the GS can be described using the VB scheme given in Scheme 2.

The substituent effect on the ESR **g** tensor components (Figure 7) is operative following different mechanisms (eqs 2−4 for instance) and cannot be rationalized in a simple way. Depending on its nature, the X group modifies the energies and the atomic composition of the frontier MO's. Our computations suggest that the former effect prevails along the **1a**-$H^+$−**1k**-$H^+$ series. Qualitatively, the $g_3$ tensor component is principally responsible for the deviation of the $g_{iso}$ value from the free electron value, and this deviation can be traced back to the fact that the SOMO and SOMO − 1 are close in energy in these compounds.

**Conclusion.** We report here the isolation and characterization of several members of a family of Fe(III) radical cations of the formula [($\eta^2$-dppe)($\eta^5$-$C_5Me_5$)Fe-(C≡C)-1,4-($C_6H_4$)X][$PF_6$] (**1a**[$PF_6$]−**1j**[$PF_6$]). These compounds are $S = {}^1/_2$ compounds, with the unpaired spin residing mostly on the {Fe−(C≡C)-1,4-($C_6H_4$)X} fragment. DFT computations on [($H_3P$)$_2$($\eta^5$-$C_5H_5$)Fe(C≡C)-1,4-($C_6H_4$)X]$^+$ model complexes indicate that a change in the X substituent induces a sizable change in the unpaired spin distribution within this moiety. Accordingly, the ESR data reveal that the unpaired electron presents an increasing "arylacetylide" (organic) character when the X substituent becomes more and more electron donating. The anisotropy ($\Delta g$) of the ESR signal can therefore be conveniently used to approximate the "metallic" character of the SOMO in families of structurally related complexes. The electronic substituent effect is also experimentally evidenced by means of

(50) In the corresponding LMCT excited states of $8^+$ or $9^+$, an electron is removed from an acetylide $\pi$-bonding MO to be promoted either into an acetylide antibonding $\pi^*$ MO[49] or into a nonbonding metal-centered d MO,[8] resulting in a diminished acetylide bond order and $\nu$(C≡C) value.

(51) Kanis, D. R.; Ratner, M. A.; Marks, T. J. *Chem. Rev.* **1994**, *94*, 195−242. di Bella, S.; Fragala, I.; Marks, T. J.; Ratner, M. A. *J. Am. Chem. Soc.* **1996**, *118*, 12747−12751.

correlations between $\sigma^+$ ESPs and the ESR rhombic **g** tensors, which emphasize the "mesomeric" origin of this phenomenon. Electronic transitions appear to be quite substituent dependent as well. Notably, a weak absorption is detected in the near-IR range for all Fe(III) complexes. We assign it to a SOMO − 2/SOMO electronic transition presenting a slight but increasing MLCT character for the most electron-releasing X substituents. Similar LF transitions also show up at higher energies in the visible range, as well as intense LMCT transitions. In conclusion, this study rationalizes the electronic properties of electron-rich mononuclear Fe(III) radicals such as **1a**$^+$−**1k**$^+$ and will now constitute a valuable benchmark to analyze spectral data for related polynuclear complexes containing [($\eta^2$-dppe)($\eta^5$-$C_5Me_5$)Fe(C≡C)-1,4-($C_6H_4$)]$^+$−fragments.

## Experimental Section

**General Data.** All manipulations were carried out under an inert atmosphere. Solvents or reagents were used as follows: $Et_2O$ and *n*-pentane, distilled from Na/benzophenone; $CH_2Cl_2$, distilled from $P_2O_5$ and then $Na_2CO_3$ and purged with argon; $HN(^iPr)_2$, distilled from KOH and purged with argon; aryl bromides (Acros, >99%), opened/stored under Ar. The [($\eta^5$-$C_5H_5)_2$Fe][$PF_6$] ferrocenium salt,[52] the Fe(II) acetylide complexes ($\eta^5$-$C_5Me_5$)($\eta^2$-dppe)FeC≡C($C_6H_4$)X (X = $NO_2$, CN, $CF_3$, Br, F, H, Me, $^t$Bu, OMe, $NH_2$, $NMe_2$; **1a**−**k**), and some of the Fe(III) acetylide complexes [($C_5Me_5$)($\eta^2$-dppe)FeC≡C($C_6H_4$)X]-[$PF_6$] (X = $NO_2$, H, $NH_2$) were prepared by previously published procedures.[1,4,14] Transmittance FTIR spectra were recorded using a Bruker IFS28 spectrometer (400−4000 $cm^{-1}$). Near-infrared (near-IR) spectra were recorded using a Bruker IFS28 spectrometer, using a Nernst Globar source and a KBr separator with a DTGS detector (400−7500 $cm^{-1}$) or tungsten source and a quartz separator with a Peltier-effect detector (5200−12500 $cm^{-1}$). Liquid near-IR spectra were recorded on a Cary 5 spectrometer. UV−visible spectra were recorded on an UVIKON XL spectrometer. EPR spectra were recorded on a Bruker EMX-8/2.7 (X-band) spectrometer. Elemental analyses were performed at the "Service central d'analyses" (USR CNRS 59 at Lyon-Vernaison) and at the "Centre Regional de Mesures Physiques de l'Ouest" (CRMPO, University of Rennes 1).

**Synthesis of the Fe(III) Acetylide Complexes.** [Fe($\eta^5$-$C_5H_5)_2$][$PF_6$] (0.95 equiv; 0.120 g, 0.361 mmol) was added to a solution of the corresponding Fe(II) parent (0.380 mmol) in 15 mL of dichloromethane, resulting in an instantaneous darkening of the solution. Stirring was maintained for 1 h at room temperature, and the solution was concentrated in vacuo to approximately 5 mL. Addition of 50 mL of of *n*-pentane allowed precipitation of a dark solid. Decantation and subsequent washing with 3 × 3 mL portions of toluene followed by 3 × 3 mL of diethyl ether and drying under vacuum yielded the desired [($\eta^2$-dppe)($\eta^5$-$C_5Me_5$)Fe−(C≡C)-1,4-($C_6H_4$)X][$PF_6$] complex as an analytically pure sample.

**[($\eta^2$-dppe)($\eta^5$-$C_5Me_5$)Fe−(C≡C)-1,4-($C_6H_4$)CN][$PF_6$] (1b-[$PF_6$]).** Yield: 92%. Color: dark brown. Crystals of the complex were obtained by slow diffusion of diethyl ether in a dichloromethane solution of the complex (layer/layer). The origin of the water solvate(s) is unknown: possibly aerial contamination during diffusion. Anal. Calcd for $C_{45}H_{43}F_6NP_3Fe·H_2O$: C, 61.52; H, 5.16; N, 1.59. Found: C, 61.30; H, 5.01; N, 1.65. IR ($\nu$, KBr/Nujol, $cm^{-1}$): 2222 (w, C≡N); 2042, 2021 (vw, C≡C).

**[($\eta^2$-dppe)($\eta^5$-$C_5Me_5$)Fe−(C≡C)-1,4-($C_6H_4$)$CF_3$][$PF_6$] (1c-[$PF_6$]).** Yield: 87%. Color: brown. Anal. Calcd for $C_{45}H_{43}F_9P_3Fe$: C, 59.82; H, 4.80; F, 18.92. Found: C, 59.60; H, 4.77; F, 16.71. IR ($\nu$, KBr/Nujol, $cm^{-1}$): 2041 (vw, C≡C).

**[($\eta^2$-dppe)($\eta^5$-$C_5Me_5$)Fe−(C≡C)-1,4-($C_6H_4$)Br][$PF_6$] (1d-[$PF_6$]).** Yield: 87%. Color: dark brown. Crystals of the complex were obtained by slow diffusion of *n*-pentane in a dichloromethane solution of the complex (layer/layer). Traces of methanol were also present in the *n*-pentane. Anal. Calcd for $C_{45}H_{43}BrF_6P_3Fe·CH_3OH$: C, 57.13; H, 5.11. Found: C, 56.88; H, 5.02. IR ($\nu$, KBr/Nujol, $cm^{-1}$): 2021, 1993 (w, C≡C).

**[($\eta^2$-dppe)($\eta^5$-$C_5Me_5$)Fe−(C≡C)-1,4-($C_6H_4$)F][$PF_6$] (1e-[$PF_6$]).** Yield: 81%. Color: dark brown. Anal. Calcd for $C_{45}H_{43}F_7P_3Fe·H_2O$: C, 60.61; H, 5.21. Found: C, 60.30; H, 5.06. The origin of the water solvate(s) is unknown, possibly aerial contamination during recrystallization. IR ($\nu$, KBr/Nujol, $cm^{-1}$): 2015 (m, C≡C).

**[($\eta^2$-dppe)($\eta^5$-$C_5Me_5$)Fe−(C≡C)-1,4-($C_6H_4$)Me][$PF_6$] (1g-[$PF_6$]).** Yield: 83%. Color: pale brown. Crystals of the complex were obtained by slow diffusion of diethyl ether in a dichloromethane solution of the complex (layer/layer). Anal. Calcd for $C_{45}H_{46}F_6P_3Fe·H_2O$: C, 62.30; H, 5.58; P, 10.71. Found: C, 62.70; H, 5.53; P, 10.57. IR ($\nu$, KBr/Nujol, $cm^{-1}$): 2001 (w, C≡C).

**[($\eta^2$-dppe)($\eta^5$-$C_5Me_5$)Fe−(C≡C)-1,4-($C_6H_4$)$^t$Bu][$PF_6$] (1h-[$PF_6$]).** Yield: 91%. Color: pale brown. IR ($\nu$, KBr/Nujol, $cm^{-1}$): 1996 (w, C≡C).

**[($\eta^2$-dppe)($\eta^5$-$C_5Me_5$)Fe−(C≡C)-1,4-($C_6H_4$)OMe][$PF_6$] (1i-[$PF_6$]).** Yield: 91%. Color: red-brown. Crystals of the complex were obtained by slow diffusion of *n*-pentane in a dichloromethane solution of the complex (layer/layer). Anal. Calcd for $C_{45}H_{46}F_6OP_3Fe$: C, 62.44; H, 5.36, F, 13.17. Found: C, 62.48; H, 5.36; F, 11.53. IR ($\nu$, KBr/Nujol, $cm^{-1}$): 1990 (m, C≡C).

**[($\eta^2$-dppe)($\eta^5$-$C_5Me_5$)Fe−(C≡C)-1,4-($C_6H_4$)$NH_2$][$PF_6$] (1j-[$PF_6$]).** Crystals of the known complex were obtained by slow diffusion of *n*-pentane in a dichloromethane solution of the complex (layer/layer).

**[($\eta^2$-dppe)($\eta^5$-$C_5Me_5$)Fe−(C≡C)-1,4-($C_6H_4$)$NMe_2$][$PF_6$] (1k-[$PF_6$]).** The oxidation reaction, the precipitation, and the washings of the Fe(III) acetylide complex were done at −70 °C. Yield: 70%. Color: dark brown. IR ($\nu$, KBr/$CH_2Cl_2$, $cm^{-1}$): 1959/1962 (vs, C≡C).

**ESR Measurements**. The Fe(III) complexes were ground with a slight excess of [($\eta^5$-$C_5H_5)_2$Fe][$PF_6$] and introduced in a ESR tube under an argon-filled atomsphere and a 1:1 mixture of degassed dichloromethane/1,2-dichloroethane was transferred to dissolve the solid, just before being frozen at 77 K, and the tubes were sealed and transferred to the ESR cavity. The spectra were immediately recorded at that temperature.

**Computational Details.** DFT calculations were carried out using the Amsterdam Density Functional (ADF) program.[53] The model compounds Fe($\eta^5$-$C_5H_5$)($PH_3)_2$(C≡C-1,4-$C_6H_4$X)$^{n+}$ (X = $NO_2$, CN, H, OMe, $NH_2$; $n$ = 0, 1) were used in order to reduce computational effort. Electron correlation was treated within the local density approximation (LDA) in the Vosko−Wilk−Nusair parametrization.[54] The nonlocal corrections of Becke[55] and of Perdew[56] were added to the exchange and correlation energies, respectively. The numerical integration procedure applied for the calculations was developed by te Velde et al.[53] The basis set used for the metal atom was a triple-ζ Slater-type orbital (STO) basis for Fe 3d and 4s and a single-ζ function for 4p of Fe. A triple-ζ STO basis set was employed for H 1s and for 2s and 2p of C, N, and O, extended

(52) Connelly, N. G.; Geiger, W. E. *Chem. Rev.* **1996**, *96*, 877−910.

(53) (a) te Velde, G.; Bickelhaupt, F. M.; Fonseca Guerra, C.; van Gisbergen, S. J. A.; Baerends, E. J.; Snijders, J.; Ziegler, T. *Theor. Chim. Acc.* **2001**, *22*, 931−967. (b) Fonseca Guerra, C.; Snijders, J.; te Velde, G.; Baerends, E. J. *Theor. Chim. Acc.* **1998**, *99*, 391−403. (c) ADF2002.01. In *Theoretical Chemistry, Vrije Universiteit: Amsterdam*; 2002 ed.; SCM: Amsterdam, The Netherlands, 2002.

(54) Vosko, S. D.; Wilk, L.; Nusair, M. *Can. J. Chem.* **1990**, *58*, 1200−1211.

(55) (a) Becke, A. D. *J. Chem. Phys.* **1986**, *84*, 4524−4529. (b) Becke, A. D. *Phys. Rev. A* **1988**, *38*, 3098−3100.

(56) (a) Perdew, J. P. *Phys. Rev. B* **1986**, *33*, 8822−8824. (b) Perdew, J. P. *Phys. Rev. B* **1986**, *34*, 7406.

with a single-ζ polarization function (2p for H; 3d for C, N, and O) for X groups. The valence orbitals of the atoms of the other groups ($C_5H_5$, $PH_3$) were described by a double-ζ STO basis set. Full geometry optimizations (assuming $C_1$ symmetry) were carried out on each complex, using the analytical gradient method implemented by Verluis and Ziegler.[57] Spin-unrestricted calculations were performed for all the considered open-shell systems. The representations of the molecular orbitals were done using MOLEKEL4.1.[58]

**Crystallography.** Crystals of **1b**[$PF_6$], **1d**[$PF_6$], **1f**[$PF_6$], **1g**[$PF_6$], **1h**[$PF_6$], **1i**[$PF_6$], and **1j**[$PF_6$] were obtained as described above. The samples were studied on a NONIUS Kappa CCD with graphite-monochromatized Mo Kα radiation. The cell parameters are obtained with Denzo and Scalepack with 10 frames (ψ rotation: 1° per frame).[59] The data collection[60] ($2\theta_{max}$, number of frames, Ω rotation, scan rate, and *hkl* range as given in Table 1) gives 69 005, 39 693, 59 451, 40 464, 76 089, 41 000, and 51 541 reflections for **1b**[$PF_6$], **1d**[$PF_6$], **1f**[$PF_6$], **1g**[$PF_6$], **1h**[$PF_6$], **1i**[$PF_6$], and **1j**[$PF_6$], respectively. Data reduction with Denzo and Scalepack[59] gave the independent reflections (Table 1). The structures were solved with SIR-97, which reveals the non-hydrogen atoms.[61] After anisotropic refinement, the remaining atoms were found by a Fourier difference map. The whole structures were then refined with SHELXL97[62] by full-matrix least-squares techniques (use of $F^2$ magnitude; $x$, $y$, $z$, $\beta_{ij}$ for Fe, P, C, N, and/or O atoms, $x$, $y$, $z$ in riding mode for H atoms with variables "*N*(var)", observations and "*w*" used as defined in Table 1).

Atomic scattering factors were taken from the literature.[63] ORTEP views of **1b**[$PF_6$], **1d**[$PF_6$], **1f**[$PF_6$], **1g**[$PF_6$], **1h**[$PF_6$], **1i**[$PF_6$], and **1j**[$PF_6$] were realized with PLATON98.[64] All of the calculations were performed on a Pentium NT Server computer.

**Acknowledgment.** Thanks are expressed to P. Hamon for kindly providing spectral data as well as starting material for the hydride complex. The CNRS is acknowledged for financial support.

**Supporting Information Available:** Tables of solvent-induced shifts on the near-IR absorption for **1f**[$PF_6$], tables of $R^2$ indices for various correlations between spectroscopic data and ESP sets, derivation of the expression for the **g** tensor components, selected plots of the energy vs **g** tensor diagonal components, and full details of the X-ray structure of **1b**[$PF_6$], **1d**[$PF_6$], **1f**[$PF_6$], **1g**[$PF_6$], **1h**[$PF_6$], **1i**[$PF_6$], and **1j**[$PF_6$], including tables of atomic positional parameters, bond distances and angles, anisotropic and isotropic thermal displacement parameters; X-ray data are also given as CIF files. This material is available free of charge via the Internet at http://pubs.acs.org.

OM0505108

(57) Verluis, L.; Ziegler, T. *J. Chem. Phys.* **1988**, *88*, 322−328.
(58) Flükiger, P.; Lüthi, H. P.; Portmann, S.; Weber, J. Swiss Center for Scientific Computing (CSCS), 2000−2001.
(59) Otwinowski, Z.; Minor, W. In *Methods in Enzymology*; Carter, C. W., Sweet, R. M., Eds.; Academic Press: London, 1997; Vol. 276, pp 307−326.
(60) Nonius, B. V. Kappa CCD Software; Enraf-Nonius, Delft, The Netherlands, 1999.
(61) Altomare, A.; Burla, M. C.; Camalli, M.; Cascarano, G.; Giacovazzo, C.; Guagliardi, A.; Moliterni, A. G. G.; Polidori, G.; Spagna, R. *J. Appl. Chem.* **1998**, *31*, 74−77.
(62) Sheldrick, G. M. SHELX97-2: Program for the Refinement of Crystal Structures; University of Göttingen, Göttingen, Germany, 1997.
(63) Reidel: D. *International Tables for X-ray Crystallography*; Kynoch Press: Birmingham, U.K., 1974; Vol. IV (present distributor: D. Reidel, Dordrecht, The Netherlands).
(64) Spek, A. L. PLATON. A Multipurpose Crystallographic Tool; Utrecht University, Utrecht, The Netherlands, 1998.